UNIVERSITY OF CALIFORNIA
RIVERSIDE

Synthesis and Processing of Iron (III) Oxide/Silica Nanopowder and Nanocomposite Structures

A Thesis submitted in partial satisfaction
of the requirements for the degree of

Master of Science

in

Materials Science and Engineering

by

Kyle Tong-Yuen Chan

December 2014

Thesis Committee:

Dr. Javier E. Garay, Chairperson
Dr. Masaru Rao
Dr. Lorenzo Mangolini

The Thesis of Kyle Tong-Yuen Chan is approved:

_____

_____

_____

Committee Chairperson

University of California, Riverside

Acknowledgements

I would like to dedicate this work to my mother, Barbara Tam-Chan for always supporting me and raising me with the tools and motivation to succeed, my father Kin-Chung Chan for being my first introduction to the world of science, my brother Keith T. Chan for never allowing me to falter in reaching my goals, and finally all my friends who have supported me.

Without the guidance and support of my advisors, Dr. Javier Garay and Dr. Yasuhiro Kodera. Dr. Kodera's contributions to the project were invaluable, especially in teaching me about the chemistry necessary to complete the bulk of my work. Also, without the many knowledgeable members of AMPS Lab – Alexander Dupuy, Andrew Wieg, Corey Hardin, Dr. Jason Morales, Anthony Fong, Aleksey Volodchenkov, and Elias Penilla– the completion of my research and studies would not have been possible. Furthermore, the help of undergraduate researchers such as Christian Niño, Jesus Gonzalez, and Matthew Duarte in completing much of the building projects necessary for research was invaluable.

ABSTRACT OF THE THESIS

Synthesis and Processing of Iron (III) Oxide/Silica Nanopowder and Nanocomposite Structures

by

Kyle Tong-Yuen Chan

Master of Science, Graduate Program in Materials Science and Engineering
University of California, Riverside, December 2014
Dr. Javier E. Garay, Chairperson

The composite material system of Iron (III) Oxide (Fe_2O_3) and Silica (SiO_2) was explored due to the unique magnetic properties of Iron (III) Oxide along with the optical properties of Silica. Through a highly controllable and tunable chemical synthesis method utilizing reverse-micelle/sol-gel processes, phase and morphology of Iron (III) Oxide nanoparticles was controlled through variation of calcination temperature from 800ºC - 1100ºC. Four polymorphs of Iron (III) Oxide were observed. Furthermore, core-shell structures comprised of iron oxide cores and silica shells were created with relatively high initial iron oxide concentrations, and densified via Current Activated Pressure Assisted Densification (CAPAD). The densified core-shell were highly transparent despite mismatches in index of refraction of iron oxide and silica, and high initial concentrations of iron oxide.

Table of Contents

List of Figures

Chapter 1 – Iron (III) Oxide Polymorphs and Stability

1.1 Introduction and Motivation

Magnetic materials have been useful throughout history in technological applications. Modern day examples are power generation and data storage. Materials with combined optical and magnetic functionalities have also been useful. For example, using the Faraday Effect, transparent materials with a high magnetic response can control the behavior of electromagnetic radiation, or light[1]. Technological applications exploiting the Faraday Effect and/or other magneto-optic effects, include magnetic switching for waveguide applications, polarization for screening of specific wavelengths, and optical diodes.

Iron Oxides are, both historically and today, one of the most-utilized material systems due to the relatively high abundance, especially in comparison to rare-earths and other state-of-the-art materials. Furthermore, while the most common crystallographic polymorph of Iron Oxide is hematite (rust), Iron (III) Oxide or Fe_2O_3 exists as four distinct polymorphs with unique magnetic characteristics. Specifically, the polymorphs of Iron (III) Oxide each exhibit unique magnetic characteristics, which may be utilized either by themselves or as composites in a wide variety of magnetic applications. To fully leverage their potential, controllability and tunability in a bottom-up synthesis process are crucial. However, due to the metastability of three of the four polymorphs of Iron (III) Oxide, synthesis and processing of either powder or bulk systems must be well-controlled. By understanding and controlling the thermodynamics and kinetics involved

of the material system, it is possible to synthesize a starting material of desired phase and morphology and to densify bulk composites with interesting and unique properties.

1.2 Historical Perspective

Historically, naturally occurring permanent magnets have had a major impact on the course of human civilization. One of the earliest known discoveries of naturally occurring magnetic materials was in ancient Greece[2] by Thales of Miletus in approximately 385 B.C., comprised of Fe_3O_4, known in modern times as magnetite. While earlier explanations of magnetic fields relied on the presence of gods or supernatural powers, by the era of Lucretius (98 B.C. – 55 B.C.), the concept of atoms had been introduce, albeit still with a degree of supernatural influences. By the late 1200's A.D., the use of permanent magnets in compasses for navigation (credited to the Chinese) had begun to spread. Over the course of several hundred years, gradual research into the scientific basis for magnetism culminated in the laws, equations, and relations developed by such well-known scientists as Carl Freidrich Gauss, Jean-Baptiste Biot, Felix Savart, Michael Faraday, and James Clerk Maxwell in 19^{th} century[2]. Modern scientific understanding of electromagnetism has paved the way for much of the technologies currently used throughout the world.

1.3 Basis for Magnetism in Materials

Magnetism is an intrinsic aspect of all materials due to the direct quantum mechanical relation of magnetic moments to lepton spin direction (± ½). A spinning charged particle (i.e. a negatively charged lepton such as an electron) will necessarily generate a magnetic dipole moment (μ) that is directly proportional to the spin angular momentum (S) by a constant factor known as the gyromagnetic ratio (γ).

$$\mu = \gamma S \quad (1.3.1)[3]$$

The gyromagnetic ratio is a particle-specific constant, and is described in a classically charged body rotating about a central axis as

$$\gamma = \frac{q}{2m} \quad (1.3.2)[3]$$

In which q is the charge, and m is the mass of the particle. With classical permanently magnetic materials, an overall magnetization is generated due to the mismatch of electron spins, and the degree to which a material is magnetized in a certain direction is known as magnetic anisotropy. Heavily anisotropic materials will tend to remain in its magnetized state until a sufficiently large external energy (field, temperature, kinetics) to change it. Examining an isolated electron with a specific spin angular momentum, a magnetic moment is generated, and the gyromagnetic ratio for such an isolated system becomes

$$\gamma = g_e \mu_B / \hbar \quad (1.3.3)[3]$$

where g_e is the g-factor, a dimensionless proportionality constant relating the magnetic moment with the angular momentum and the Bohr Magneton (μ_B = 9.274 x 10^{-24} J/T, a physical constant which describes the units of an electron magnetic dipole moment)[3]. Furthermore, a stationary charged particle in the presence of an external magnetic field (B), a torque (τ) is generated due to the interaction between an intrinsic magnetic moment and the applied field, in a process known as Larmor Precession.

$$\tau = \mu \times B \quad (1.3.4)$$

Magnetic materials, regardless of morphology or composition, behave as magnetic dipoles, analogous to Coulombic interactions in electrostatics[4], in which two interacting magnetic poles (p_1 and p_2) interact, with each pole generating a force acting on the other.

$$F = \frac{p_1 p_2}{4\pi\mu_0 r^2} \quad (1.3.5)$$

The presence of such a dipole interaction is present in both permanent and electro magnets. Expanding further upon such concepts, magnetic fields generated by such dipole interactions can be described most simply as field strength and field density. A magnetic field can be generated by either a current (moving charges) or by pole interaction, and is commonly denoted as H, with units of Oersted (Oe) or Amperes per meter (A/m). In the case of an induced magnetic field due to a current, the generated field, in a simple case of a straight wire, is equivalent to

$$B = \frac{\mu_0}{4\pi}\frac{I}{R}(sin\theta_2 - sin\theta_1) \quad (1.3.6)$$

where μ_0 is the permeability, I is the current, R is the distance from the primary axis, and θ_1 and θ_2 are the angles between the point at which the field is measured and the initial reference (starting point) of the wire, and the desired distance along the wire, respectively. The magnetic field flux density is typically denoted as B, with units of Tesla (T) or Gauss (G). Magnetic field flux density (B) and magnetic field intensity (H) are commonly related with

$$B = \mu_0(H + M) \quad (1.3.7)$$

In which μ_0 is a material constant known as permeability, or the ability for a material to generate a magnetic field throughout its body, and M is the magnetization, or magnetic moment per volume. The value M is determined for individual materials based on a dimensionless quantity known as magnetic susceptibility (χ), which describes the ability for a material to be magnetized in response to an externally applied field H_0[4].

$$M = \chi H_0 \quad (1.3.8)$$

Using magnetic susceptibility values, it is possible to classify magnetic behavior in materials as diamagnetic, paramagnetic, antiferromagnetic, ferrimagnetic, and ferromagnetic.

1.4 Types of Magnetic Materials

Diamagnetic materials are the most common form of magnetic material, with susceptibility values that are negative, and magnitudes typically less than 10^{-5}, and are considered weakly magnetic. In the majority of materials, diamagnetism exists to some degree due to the orbital momentum of electrons creating an effectively induced field due to the presence of moving charges (analogous to a current loop generating a magnetic field). When an external field is applied to a diamagnetic material, a magnetic flux in opposition to the applied field is generated, producing a magnetic moment response directly antiparallel to the external field.

Paramagnetism is a form of magnetism which arises due to the presence of unpaired and delocalized dipoles. Due to the random orientation of magnetic sites, a paramagnetic material exhibits little to no anisotropy without the influence of external forces. However, when an external field is applied, a consequence of these delocalized moments is that the material will respond linearly with the external field, and subsequently return to a randomly magnetized state when the external field is removed. The permeability of such materials is typically around or slightly greater than 1, and changes with temperature.

Antiferromagnetic materials contain a series of directly opposing, antiparallel magnetic moments, and thus exhibit no net magnetization in any direction. Such materials typically have very low magnetic susceptibilities, and react strongly to resist the effects of an externally applied magnetic field. Meanwhile, ferromagnetic materials contain magnetic moments which align readily in a specific direction (high anisotropy) and have a tendency

to maintain this net magnetization. The moments of a ferromagnetic material continuously align with an external field until it reaches a point known as the saturation magnetization, or the finite limit of magnetization which can occur due to the full-alignment of moments. A highly ferromagnetic material can have magnetic susceptibility in the range of 10^6. The maintenance of the magnetically aligned state in ferromagnetic materials is due to the close-knit interaction of the moments throughout the material, otherwise known as exchange interaction. At sufficiently high temperatures, all ferromagnetic materials decompose into a randomly oriented state where exchange interaction does not occur, and becomes paramagnetic. Ferrimagnetism, meanwhile, is somewhat of a cross between antiferromagnetism and ferromagnetism, in which the distribution of moments is such that a certain amount of moments will be aligned, while some moments are in opposition. However, the unequal number of opposing moments allows for an overall magnetization to occur, in a behavior very similar to ferromagnetism[4].

1.5 Permanent Magnets

Magnetism, being an inherently hysteretic (non-linear) behavior due to moment rotation and domain interactions (clusters of aligned magnetic moments within the material) under externally applied fields, is often experimentally characterized[2]. In considering a permanent magnet, along with magnetic susceptibility, other material-dependent values include saturation magnetization, remanence, and coercivity. Saturation magnetization, as previously stated, is directly related to magnetic susceptibility and is

dependent on the degree to which magnetic moments can align. A paramagnetic or antiferromagnetic material will typically be unable to reach a saturation point unless a sufficiently high field is applied, while a ferri- or ferromagnetic material will readily saturate. Similarly, when the external field is removed, the different forms of magnetic materials will behave differently, where ferri/ferromagnetic materials will maintain their magnetization, while diamagnetic or paramagnetic materials will spontaneously reorient randomly. The degree to which a material is capable of maintaining its magnetization in the absence of an applied field is known as *remanence*. Materials that are capable of maintaining a magnetization without an external field also exhibit a degree of resistance to demagnetization, where the amount of an external field in the opposite direction to its magnetization needed to bring the overall moment to zero is known as *coercivity*, or *coercive field*.

Permanent magnets, being considered either "soft" or "hard", exhibit either high remanence or coercivity, respectively. An ideal permanent magnet will exhibit both high remanence and coercivity, meaning that the moments can be readily aligned in a certain direction, while simultaneously resisting demagnetization from an external field. To accomplish this, multiple magnetic phases may be incorporated in a permanent magnet such that a "hard" material may interact with a "soft" material, displaying the qualities of both, in a process known as exchange coupling. The interaction of hard and soft magnetic phases is dependent on the interaction between the moments of each phase, and can be described in terms of energy.

$$U_{ij} = -2JS_i \cdot S_j \text{ (1.5.1)}$$

Where U_{ij} is the potential energy of the spin moments of two atoms (S_i and S_j), and J is the exchange integral. The most stable state of such an exchange is one in which the moments are parallel, energy as at a minimum, and the exchange integral is positive

1.6 Thermodynamics Stability of Iron (III) Oxide Polymorphs

Iron (III) Oxide has been reported to exist in the α–, β–, γ–, and ε– phases[5], with a theoretical δ– phase[6]. It is well understood that the stability of materials in certain phases is heavily dependent on time and temperature, as specific crystal structures may be more energetically favorable at specific ranges, giving rise to the concept of metastability[7]. In the case of Iron (III) Oxide, the most common, naturally occurring, and stable form is the α–phase, more commonly known as hematite, followed by the metastable γ–phase, known by the mineral name of maghemite. Two additional phases, the β–, and ε– phases, have been synthesized in laboratories using various synthesis routes, but are reported to be extremely thermodynamically unstable, readily transforming into the α–phase upon application of heat[5][8]. Each phase is crystallographically distinct, with the α–phase existing as a hexagonal rhombohedral, γ–phase as an inverse spinel, β–phase as a body-centered cubic, and the ε–phase as a complex orthorhombic structure (figure 1.6.1).

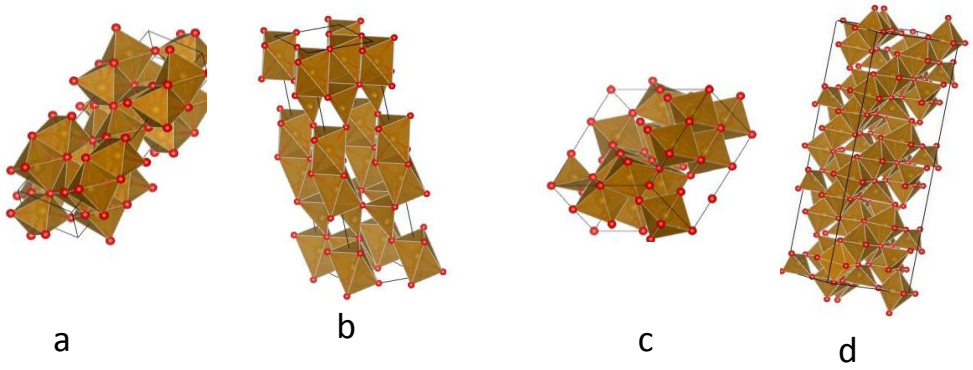

Figure 1.6.1 Iron Oxide (a) α (b) β (c) ε (d) γ phases, structures generated via VESTA Software

Consequently, while thermodynamics affect the crystal structure of Iron (III) Oxide, the crystal structures further affect the magnetic properties of the compound. To understand the relation between thermodynamics, crystal structure/polymorphism, and magnetic properties, it is important to begin with a conceptual discussion of thermodynamics.

In discussing thermodynamics, both entropy and enthalpy must be considered to fully explain the behavior of a system. Entropy, conceptually, is the measure of disorder in a system, while enthalpy can be considered to be the energy of a system, both internal and potential. These concepts can be represented mathematically as

$$\Delta S = \int \frac{dQ}{T} \quad (1.6.1)$$

$$H = U + pV \quad (1.6.2)$$

where S and P are entropy and enthalpy, respectively, and dQ is change in heat of the system, T is temperature, U is internal energy, p is pressure, and V is volume. To relate both entropy and enthalpy, the concept of Gibbs Free Energy is introduced, which in

essence quantifies the usefulness or availability of energy in a system, and is represented mathematically as a relation between entropy, enthalpy, and temperature

$$\Delta G = \Delta H - T\Delta S[7] \quad (1.6.3)$$

It can then be stated that with the inclusion of both entropy and enthalpy, the Gibbs Free Energy demonstrates the overall stability of a system at specific temperatures, where a higher entropy/lower enthalpy, or a more negative Gibbs Free Energy, is a preferred state for a system. Because such a behavior is non-linear among the various phases of a material, stability of phases is heavily dependent on temperature ranges, allowing for metastable phases to exist.

With a general understanding of the relation between Gibbs Free Energy and the stability of a system, it is then important to consider the relation between thermodynamics and crystal structures of the various Iron (III) Oxide Phases. Crystal structures, being comprised of some combination of the seven Bravais Lattices, vary in overall stability as a consequence of the effects of bond angles and energies[9][10]. Stability of a particular molecular is determined by the combination of all attractive and repulsive forces (i.e. bond type versus Van Der Waal's forces). As a consequence, the crystal structure of a particular substance tends to be comprised of the most energetically favorable repeating sequence of molecular bonds. Due to the changing behavior of chemical bonds in relation to the overall enthalpy and entropy of a system, there is a direct thermodynamic effect on the stability of various crystal structures.

In many materials, this also translates to a relation between Gibbs Free Energy and particle size[11]. The stability of a system is also heavily dependent on the availability of interactive surfaces. Essentially, the same material at two different size scales (nanoscale grains versus micron sized grains) will vary in stability due to the overall surface area to mass ratio. Hence, a nanoscale material may undergo certain reactions to reach a more stable state, such as agglomeration and a series of phase transitions. Furthermore, a finite number of crystal structure combinations are possible due to the limitations imposed by thermodynamics, kinetics, and overall energy states of atoms, allowing for a particular molecule to exist only in a discrete number of crystallographic structures.

With the Iron (III) Oxide material system, the α–phase is most abundantly occurring in nature, followed by the metastable γ-phase, then rarely-occurring ε-phase and β– phase. Because nanoparticles tend to agglomerate, and due to the high atomic packing factor (APF) and energetically favorable hexagonal structure[9], the various metastable phases of Iron (III) Oxide (γ–, ε–, β–phases) readily convert to the α-phase at elevated temperatures (between 773º K - 1273º K). The γ–phase, or maghemite, also occurs naturally due to weathering or low-temperature oxidation reactions, and takes the form of an inverse-spinel – a derivative of the face-centered cubic structure. However, despite the similar APF of hexagonal and face-centered cubic structures, the presence of open bonds in the inverse-spinel structure cause a metastability of the γ-phase at elevated temperatures (above 873º K). The ε-phase is comprised of a complex orthorhombic

structure, in which Fe atoms occupy four non-equivalent sites, and thermodynamically can be treated as an intermediate phase between the γ– to α–phase transition[8]. Due to its structure and position during thermodynamic phase transitions, the ε-phase tends to be extremely unstable at elevated temperatures. Finally, the β-phase, comprised of a body-centered cubic structure, is similarly unstable, and tends to convert readily to the α–phase. Due to the presence of available bonding sites in the γ–, ε–, β–phases, and the overall stability of a hexagonal structure, the existence of the three metastable phases tends to be limited to the nano-sized particle regime. Consequently, the ideal particle size for each of the metastable phases can be directly related to Gibbs Free Energy (figure 1.6.2).

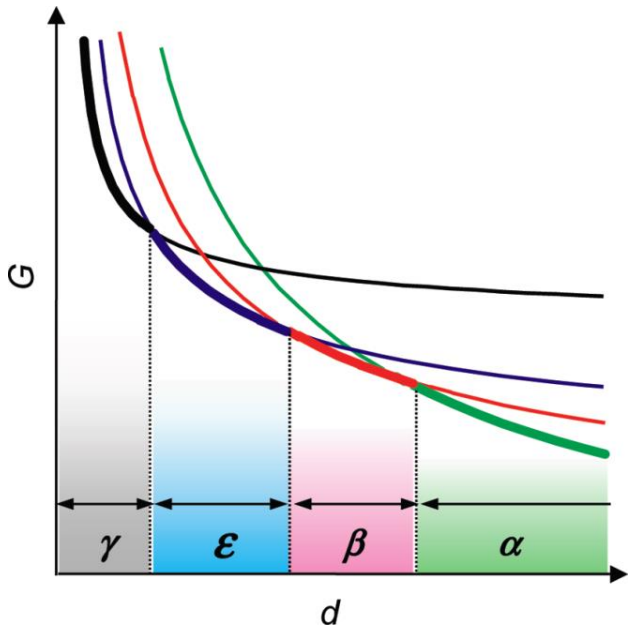

Figure 1.6.2 Gibbs Free Energy versus particle size distribution of Fe_2O_3 phases with arbitrary units[5]

With an understanding of the relation between Gibbs Free Energy, particle size, and phase stability, stabilization and isolation of specific metastable phases is possible through control of temperature and grain size. Recently, it has been reported that with a mesoporous silica matrix as a grain-size limiter, all four observed polymorphs of Iron (III) Oxide have been demonstrated in sequence as a function of temperature[5].

1.7 **Unique Magnetic Properties of Iron (III) Oxide Polymorphs**

With an understanding of the thermodynamic interpretation of phase transitions, a discussion of magnetic behavior of materials is necessary. The basis of magnetism in materials stems from the sum total of electron magnetic moments of a particular material. Hence, the strength of a materials magnetic field is dependent on the overall symmetry of electron magnetic moments of the atoms involved in bonding[2]. However, magnetic behavior can vary among various phases of the same material. All materials either behave as a ferromagnet, ferrimagnet, antiferromagnet, diamagnet, or paramagnet. The observed phases of Iron (III) Oxide have been demonstrated to exhibit antiferromagnetic (α), ferrimagnetic (γ), paramagnetic (β), and canted-antiferromagnetic (ε) behavior. In a typical permanent magnet, magnetic moments are fully aligned, leading to a next magnetization in a specific direction, known as ferromagnetism. In antiferromagnetic materials, magnetic moments exist in direct opposition, leading to a next non-

magnetization. A ferrimagnetic material is one in which an unequal number of magnetic moments are in opposition, leading to a next magnetization in a certain direction despite opposing moments. A canted-antiferromagnet is one in which the sum of magnetic moments lead to an overall negation of the magnetic field, but a canting in the moments allow for magnetization of the material under sufficiently high applied field [2] (figure 1.7.1).

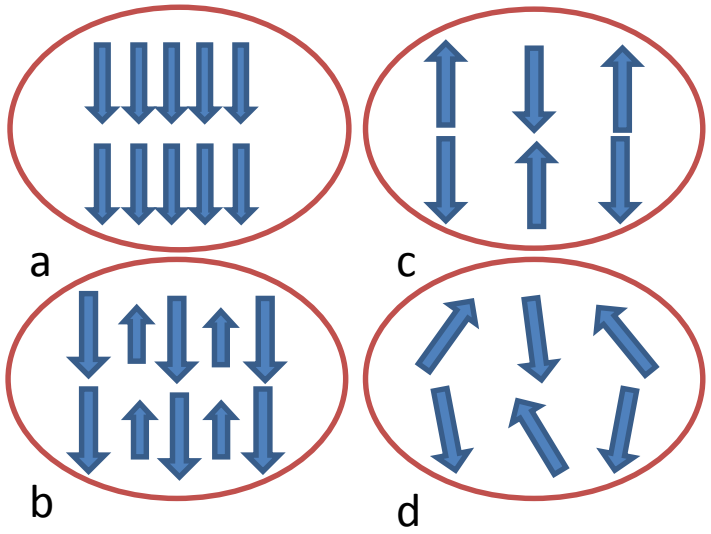

Figure 1.7.1 Schematic of typical alignment of magnetic moments in a (a) ferromagnet (b) ferrimagnet (c) antiferromagnet (d) canted-antiferromagnet

As previously stated, the crystal structures of the four observed polymorphs of Iron (III) Oxide vary in stability due to the presence of available bonding sites within the individual crystal lattices. A further consequence of the presence of such free bonds is a mismatch of magnetic moments, leading to a net magnetization[12]. In examining the

crystal structures of each phase, it is evident that in addition to thermodynamic stability, α–Fe_2O_3 demonstrates a primarily antiferromagnetic behavior, which under the influence of temperature, changes to a slight canted-antiferromagnet between the Morin temperature (T_m = 260º K) and the Neel temperature (T_N = 950º K), followed by a complete loss of magnetic ordering above the Neel temperature[13]. β–Fe_2O_3 displays antiferromagnetic behavior below, and paramagnetic behavior above T_N = 119º K. γ–Fe_2O_3 displays a Curie temperature of T_c = 928º K (and without external influence, beings a phase transition into α–Fe_2O_3 above 873º K)[14]. ε–Fe_2O_3 meanwhile, displays a transition from a paramagnetic state to an ordered canted-antiferromagnetic state at T_c = 490º K[8].

In addition to the intrinsic magnetic properties of the Iron (III) Oxide polymorphs, magnetic behavior is also determined by the size and shape of the material. Typically, the coercive field of a material increases with decreasing grain size down to the single magnetic domain, beyond which coercivity drops drastically as superparamagnetic behavior begins to dominate[15]. Besides the scaling effects that can occur due to the presence of magnetic domains, shape-control of a magnetic material can also affect the coercivity of a system. As is evidenced by the non-linear behavior of magnetic materials, the process by which magnetic domains align to a field is dependent on the structure of a material when above the single-domain size scale (figure 1.6.2).

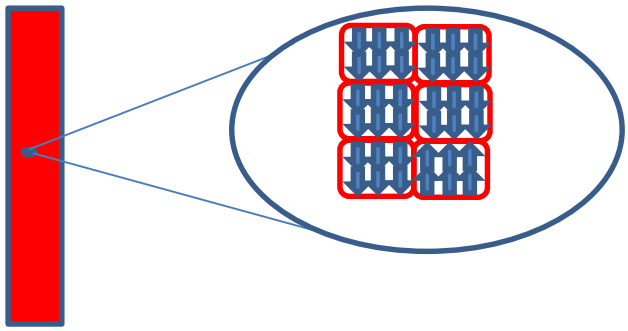

Figure 1.7.2 Schematic illustrating the morphology effect on magnetic domain behavior

1.8 Optical Transparency Dependence on Composition and Dispersion

To retain optical transparency in a composite of a highly non-transparent material within a transparent matrix, two criteria must be met. First, reaction between the two materials must be minimal to avoid doping or unwanted phases thus retaining two discrete material components. Second, very good dispersion and excellent size control of the non-transmitting material must be achieved because reducing size of the material minimizes light scattering.

The first criteria can be met by the combination of phase control at the chemical synthesis level, in conjunction with material selection. Specifically. Iron (III) Oxide, and Silica (SiO_2) were chosen specifically for the unique polymorphs of Iron (III) Oxide, the high transparency of common silica polymorphs, and the lack of interaction, or formation of ferrosilicon under the processing conditions to be used. Highly specific ratios of Iron (Fe) and Silicon (Si) are required to react within a highly oxygen-reducing atmosphere at high temperatures for prolonged periods to form stable ferrosilicon phases, and thus are

unlikely to form as the dominant structure in the synthesized and processed samples[16], [17].

The second criteria can be met through a combination of a unique chemical synthesis process as well as a rapid densification process to avoid excessive grain growth during removal of porosity. In considering the system as two separate components, not only the index of refraction, but also size scale of the materials must be determined and controlled. Specifically, the common Iron (III) Oxide phases have index of refractions of approximately n = 2.5, while common polymorphs of Silica, such as α-quartz have index of refractions around n = 1.5[18]. Due to the highly mismatched indices of refraction, large grain sizes or large aggregated clusters of the non-transparent phase within the transparent phase can contribute to large drops in transmission, in an effect akin to the refraction of polarized light passing through mismatched mediums, as described by the Fresnel equations. In the case of light passing through a plane perpendicular to its axis of polarization (s-polarization), the reflection can be calculated as

$$R_s = \left|\frac{n_1 \cos\theta_i - n_2 \cos\theta_t}{n_1 \cos\theta_i + n_2 \cos\theta_t}\right|^2 \quad (1.8.1)$$

in which R_s is the reflection coefficient (%), n_1 and n_2 are the indices of refraction for each material, θ_i is the angle of the incident light, and θ_t is the angle of the transmitted light, or angle of refraction. Similarly, the reflection coefficient of light polarized parallel to the plane of incidence (R_p) can be calculated based on a function of the angle of incidence, transmission, and the respective indices of refraction.

$$R_p = \left|\frac{n_1 \cos\theta_t - n_2 \cos\theta_i}{n_1 \cos\theta_t + n_2 \cos\theta_i}\right|^2 \quad (1.8.2)$$

Transmission, then, is a function directly related to reflection, in which the percent of transmitted light is the remainder of light not reflected.

$$T_{s,p} = 1 - R_{s,p} \quad (1.8.3)$$

It can be seen from the Fresnel equations that the non-transparent component in any optically-transmitting composite must offer a negligible contribution. The effects on transmission from the non-transparent component is analogous to that of major impurities or pores within the transparent structure. Mie and Rayleigh theory's describe the scattering effects of particles much smaller than the wavelength of light and particles equal to or larger than the wavelength of light, respectively[19].

$$I = I_0 \left(\frac{1+\cos\theta^2}{2R^2}\right)\left(\frac{2\pi}{\lambda}\right)^4 \left(\frac{n^2-1}{n^2+1}\right)^2 \left(\frac{d}{2}\right)^6 \quad (1.8.4)$$

Previous work has demonstrated a relation between transmission of light and size of pores, amount of impurities, and most importantly, the non-transmitting medium[20], [21]. Thus, high dispersion, which can be achieved during the powder synthesis process, in conjunction with preservation of nanosized particles (a scale smaller than that which will affect visible wavelengths of light), which can be achieved through rapid densification, are the two primary goals to be attained in creating transparent composites.

Chapter 2 – Synthesis and Processing of Iron (III) Oxide Nanoparticles

2.1 Chemical Synthesis of Iron-Oxide Nanoparticles

A reverse-micelle/sol-gel process was used in synthesizing ε-Fe_2O_3. The mechanism for a micelle formation relies upon the random diffusion of a surfactant into a water phase, and the adsorption onto the surface of oil and water interfaces. Typical micelle processes involve the dispersion of a surfactant - amphiphilic compounds comprised of hydrophobic heads and hydrophilic heads- in a water phase. Upon introduction of an oil phase, the tendency of the surfactant is to align such that the hydrophobic tails encapsulate the oil phase and hydrophilic heads remain in contact with the water phase. In the case of a reverse-micelle, however, the dispersion order is reversed, such that the oil phase serves as the medium while the water is encased within the aligned hydrophilic heads. A sol-gel (solution-to-gel) process is a process in which small molecules transition into solid phases, and is a common method for metal-oxide synthesis. In sol-gel processes, a metal ion solution is combined with a gel precursor, which after undergoing a hydrolosis process forms a gel. Consistency of such a formed gel can range from a near-solid substance to requiring a large amount of centrifugation and heating processes to full form the gel-like qualities.

The process, as adapted from Sakurai, et al [22] involved the preparation of two reverse-micelle solutions , containing nitrate reactants ($Fe(NO_3)_3$ (Iron nitrate) and $Ba(NO_3)_2$) (barium nitrate) in one solution (figure 2.1.1a) and NH_4OH (ammonium hydroxide) in the other (figure 2.1.1b), encapsulated within the reverse-micelles (figure

2.1.1e). Additionally, tetraethylorthosilicate (TEOS) was added as a silica precursor, which underwent a sol-gel process upon contact with atmosphere and H_2O (figure 2.1.1c and d).

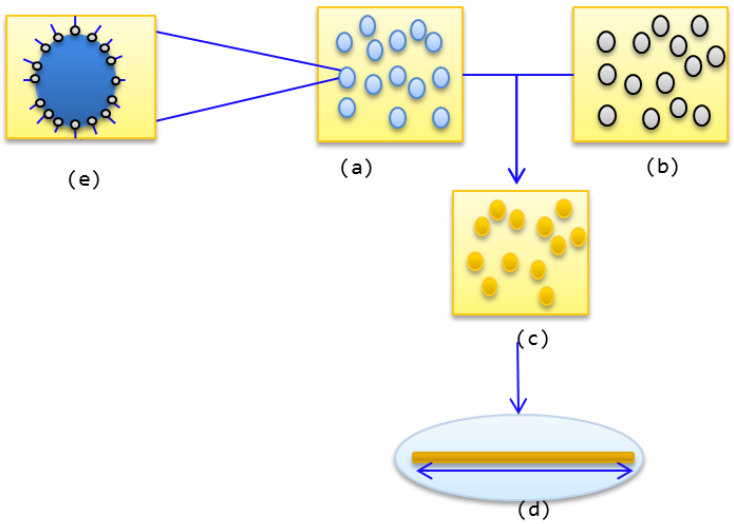

Figure 2.1.1 Diagram of reverse-micelle/sol-gel synthesis process, adapted from Sakurai, et al. [22]

Additional methods of metal-oxide nanoparticle synthesis have been reported, including the thermal decomposition of iron-containing precursors, microemulsion processes, sonochemical reactions, hydrolysis/thermolysis of iron oxide precursors, flow-injection synthesis, and electrospray synthesis[23]. However, the novelty of the reverse-micelle/sol-gel method lies in the phase-selectivity, size controllability, and homogeneity. With correct dispersion and a well-formed amorphous silica matrix, it is possible to prevent wide-spread aggregation of metal oxide nanoparticles during calcination

processes, allowing for a higher degree of controllability over both phase and morphology[8].

2.2 Synthesis Process

Prior to reverse-micelle formation, four separate solutions are prepared. Two of the solutions contain the necessary surfactants, in which 9.7 mmol of $C_{16}H_{33}N(CH_3)_3Br$ (CTAB) and 39mmol of C_4H_9OH (butyl alcohol) were slowly dispersed into 110mmol of C_8H_{18} (octane) while stirring vigorously. The two solutions were then mixed until the surfactants are well-dispersed in the octane. A third and fourth reactant solution containing 0.74 mmol of $Fe(NO_3)_3$ and 0.15mmol $Ba(NO_3)_2$ (an alkali ion source) dispersed into 330 mmol of H_2O, and 30 mmol NH_4OH added to 330 mmol H_2O , respectively, were prepared while the surfactant solutions were mixed. After thoroughly mixing, the nitrate-containing solution is added to one surfactant solution while the ammonia-containing solution is added to the second surfactant solution to form two reverse-micelle solutions (solution A and B respectively). After mixing until the solutions become translucent, solution B is slowly dripped into solution A while stirring. $Fe(OH)_3$ is formed through a hydroxylation reaction between iron nitrate and ammonium hydroxide, forming $Fe(OH)_3$ (Iron hydroxide) and NH_4NO_3 (ammonium nitrate) as a byproduct.

$$Fe(NO_3)_3 + 3\,NH_3\,(aq) \rightarrow Fe(OH)_3 + 3\,NH_4NO_3 \quad (2.2.1)$$

The expected particle size of the iron hydroxide resulting from the reaction was within the 10nm range. During the mixing/precipitation process, 6.7 mmol $Si(C_2H_5O)_4$ (TEOS), a SiO_2 (silica) precursor, is also added to the solution, reacting with H_2O to form silica and a C_2H_5OH (ethanol) byproduct.

$$Si(C_2H_5O)_4 + 2\,H_2O \rightarrow SiO_2 + 4C_2H_5OH \quad (2.2.2)$$

Upon injection of TEOS, the solution underwent a sol-gel reaction, resulting in a silica matrix forming around the Iron hydroxide particles, effectively encasing the particles to prevent aggregation[22]. In addition to the H_2O and TEOS reaction process, the presence of excess ammonium hydroxide is believed to act as a catalyst for the gel transition and resulting silica formation. The role of ammonium hydroxide as a catalyst in the TEOS hydrolosis process is likely due to the ability to contribute a hydroxyl (-OH) ion to electrophilic (positively charged) species during the reaction process[24]. After stirring for 1-2 hours, the $Fe(OH)_3$ and SiO_2 mixture is collected through centrifugation, and rinsed thoroughly with $CHCl_3$ (chloroform) and CH_3OH (methanol) to remove excess unreacted material/byproducts. The remaining powder is then dried for 24 hours at 50° C.

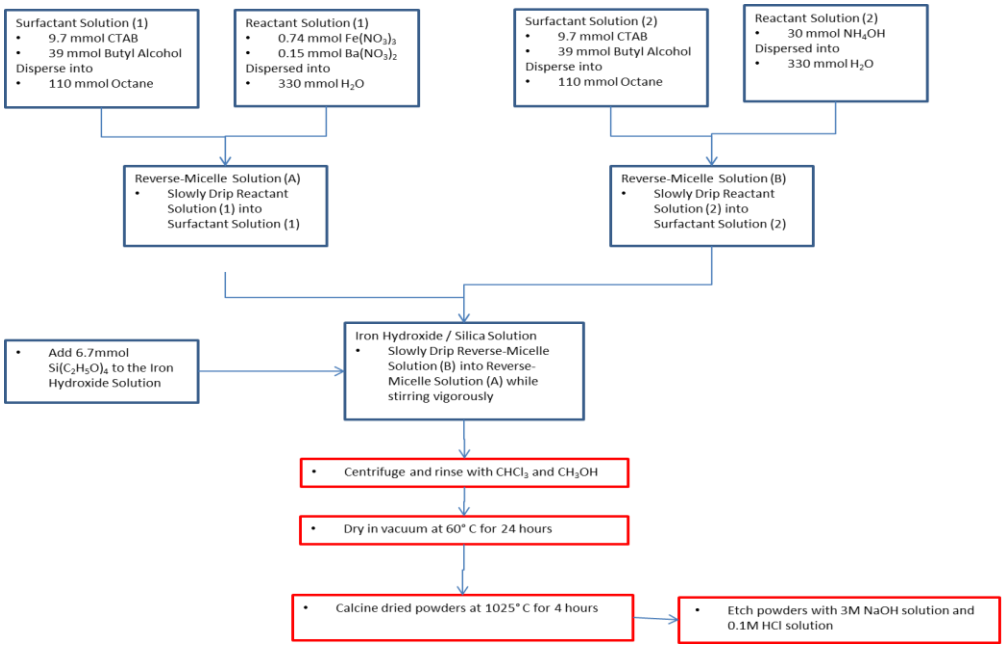

Figure 2.2.1 Detailed flow chart of synthesis and calcination process of iron oxide nanopowders

2.3 Powder Calcination/Processing

Following the drying process, the silica-encased iron hydroxide is then converted into various phases of Iron (III) Oxide through calcination at varying times and temperatures. Specific temperature ranges for phase changes were found using thermogravimetric/differential thermal analysis (TG-DTA) on a TA Instruments SDT-Q600 TGA/DSC system. Thermogravimetric/differential thermal analysis relies on both the measurement of changing heat flow and changing mass over varying time and temperature to indicate potential phase changes or reactions

With a known sample starting mass, weight gain/loss and heat flow change was measured as a function of temperature, ranging from room temperature to 1400° C in a

dry-air atmosphere. Changes in heat flow were monitored as the primary indicator for crystallographic phase change, due to the shifting of crystal structure inherently altering thermal conductivity properties. Phase transitions, as reported in literature, were predicted to occur beginning with iron hydroxide converting into iron oxide before 900° C, γ-Fe_2O_3 being the dominate phase between 900° - 1000° C, followed by ε-Fe_2O_3 forming as the majority phase between 1000° - 1150°C, which can only be formed through such a procedure, β-Fe_2O_3 being observed between 1150° - 1250° C, and α-Fe_2O_3 forming beyond 1250° C[5]. Initially, the synthesized powder was prepared for TGA directly after drying at 80°C in vacuum. A significant exothermic, weight-loss event occurred between 230° - 270° C, indicating the decomposition of a large amount of organic byproduct after the synthesis/drying process (figure 2.3.1).

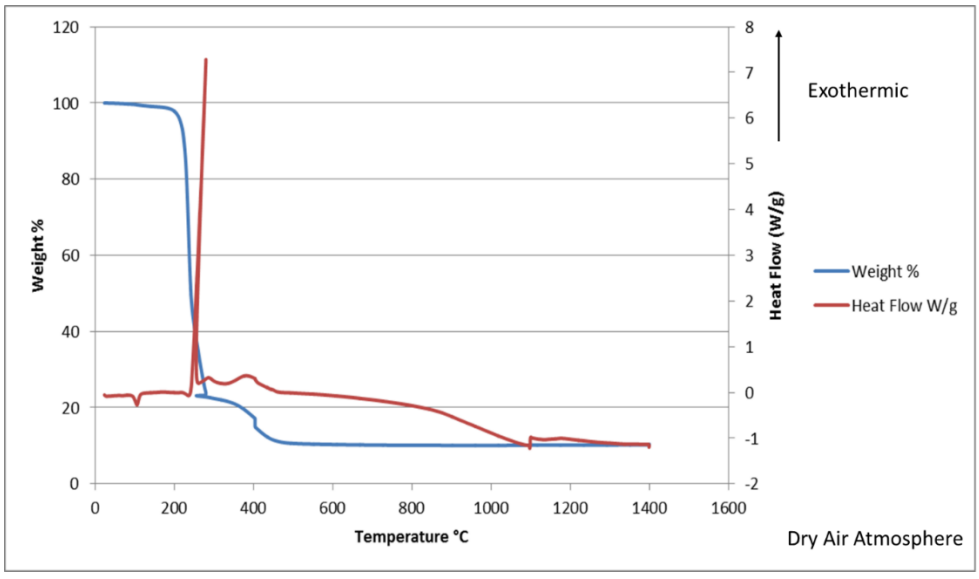

Figure 2.3.1 TG-DTA examines weight% and heat flow vs temperature of synthesized powders

Subsequent powders were annealed at 600° C in order to remove organic material prior to processing and minimize the influence of organic byproduct. Measuring weight loss/gain and heat flow of annealed powders in TGA demonstrated a minor outgassing with less than 4% weight loss, and major heat flow changes at approximately 780°, 940°, 1050°, and 1230° C (figure 2.3.2). The initial shift to an endothermic reaction at 350° C indicates both a removal of organic material and a shift from iron hydroxide into iron oxide. The changes in heat flow between 780° - 940° C indicates the transition into γ- Fe_2O_3, followed by ε-Fe_2O_3 formation peaking at approximately 1050° C, and transitioning into α- Fe_2O_3 above 1200° C. The temperatures at which changes in heat flow indicated potential crystallographic phase changes were then used as the basis for isolating the individual phases of Fe_2O_3.

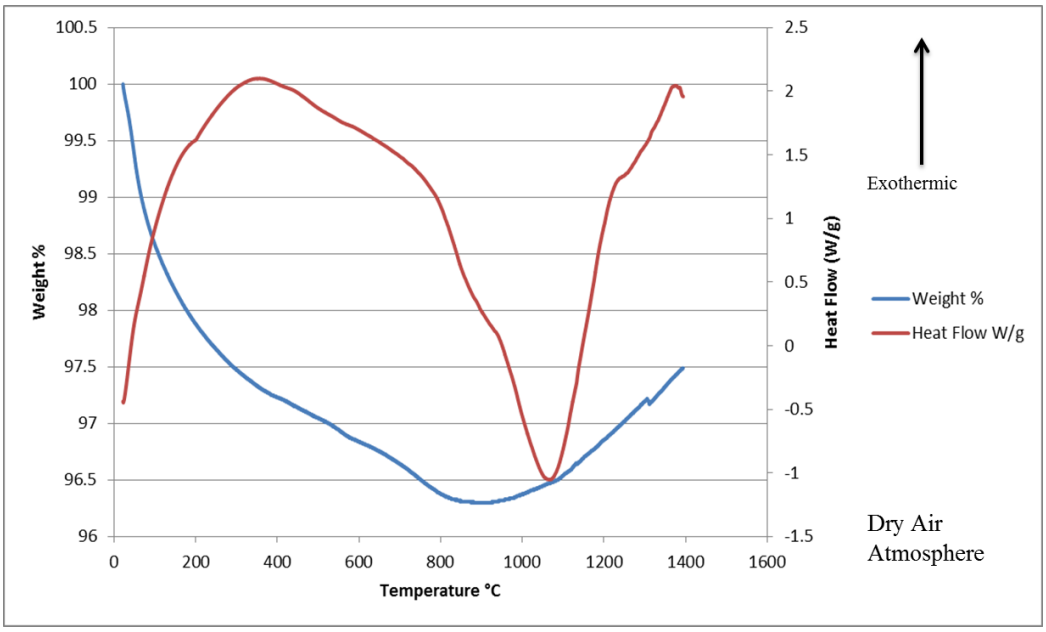

Figure 2.3.2 TG-DTA data of powders calcined at 600°C

One of the primary goals of the process was the formation of silica-encased nanorods. The mechanism for nanorod formation involves the adsorption of alkali ions (Ba^+ ions contributed by $Ba(NO_3)_2$) onto the surface of the Fe_2O_3 nanoparticles during heating along the (010) or (001) planes, forcing nanowire growth in the (100) plane[22], [25]. While the silica matrix prevents Fe_2O_3 particle diffusion and aggregation below 1000°C, SiO_2 undergoes a glass transition at 1000° C, at which point the Ba^+ ions actively limit Fe_2O_3 aggregation along the (010) and (001) planes, allowing nanowire growth of up to 1μm[22] (figure 2.3.3). At sufficiently high temperatures (above 1100° C), the Fe_2O_3 particles transition into the larger and more stable α- phase.

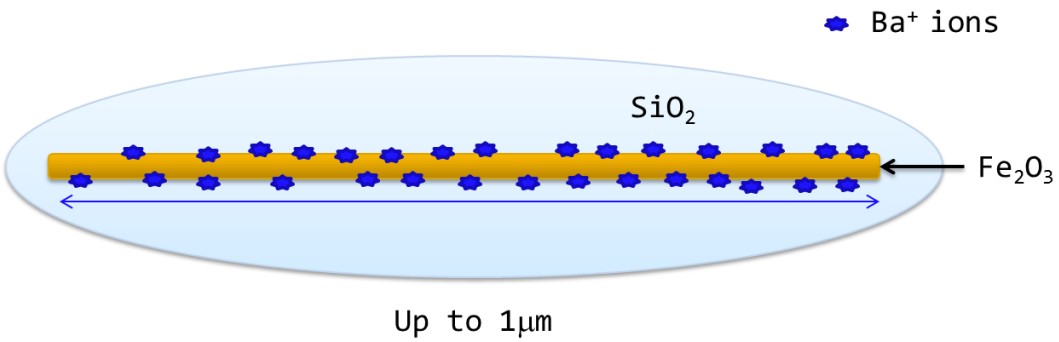

Figure 2.3.3 Schematic of iron oxide nanorods encased within a silica shell, synthesized through the reverse-micelle/sol-gel process

After processing powders at various conditions, powders were partially etched with a 1.75M KOH solution, then rinsed with a 0.1M HCl solution and H_2O in order to remove excess silica for various characterization processes.

With an understanding of the phase change process, it is possible to isolate specific phases through control of calcination time and temperature. As a consequence, due to the phase-dependent magnetic properties, it is possible to obtain magnetic nanoparticles of a specific desired size and morphology.

2.4 Silica Shell Synthesis

Core-shell structures were synthesized by first preparing a silica-precursor solution comprised of 20 mmol TEOS added to 4 mol of H_2O, 1.2 mol of Ethanol, and 0.23 mol NH_4OH. Varying amounts of the reverse-micelle solution was then measured into different containers. The silica-precursor was added to each container to create iron hydroxide core/silica shell solution with 0.01, 0.5, 1.0, and 2.5 mol% iron oxide structures. Each solution was stirred for 16 hours, then centrifuged to separate the desired powder from excess byproduct. The precipitated powder was dried for 24 hours at 80º C, then calcined at 600ºC for 4 hours to remove unwanted organic residue. The powder was then collected for characterization and densification.

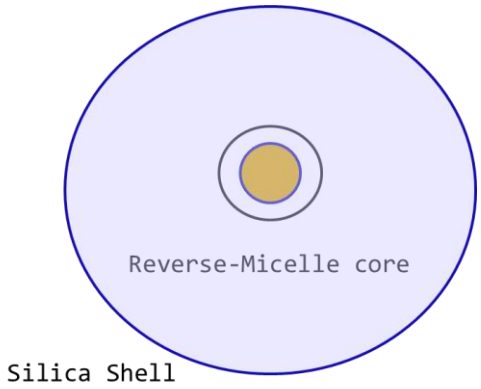

Figure 2.4.1 Simple diagram of the iron oxide core with silica shell

Chapter 3 – Powder Characterization Techniques and Results

3.1 Background on X-Ray Diffraction

A widely-used method of material characterization is X-Ray Diffraction (XRD) crystallography. All crystalline materials are comprised of a unique combination of the Bravais Lattices, and thus a unique combination of miller indices. An additional consequence of a crystalline material is that the atomic spacing is uniform throughout the material (in the absence of structural defects and abnormalities) due to the repeating periodic arrangement of lattices. X-rays, being a form of electromagnetic radiation, interact with individual atoms within a crystal lattice in a wave-particle manner, resulting in some combination of absorption, reflection, and scattering, known collectively as diffraction. Due to the wave-like nature of X-ray scattering, either constructive or destructive interference can occur. X-ray diffraction powder analysis techniques typically rely on the detection of constructive interference patterns, which was first mathematically explained by William Lawrence Bragg through Bragg's law.

$$n\lambda = 2dsin\theta \quad (3.1.1)$$

where n = 1,2,3… is the order of constructive interference, λ is the wavelength of the incident x-ray, d is the planar spacing, and θ is the angle of incidence. The planar spacing combination, being unique to each material, can be calculated for cubic systems as

$$d_{hkl} = \frac{a}{\sqrt{h^2+k^2+l^2}} \quad (3.1.2)$$

where h, k, and l are three integers denoting the miller indices which are planes orthogonal to a reciprocal lattice vector. Hexagonal and rhombohedral systems can have a fourth index number typically denoted as *i*, a redundant index in addition to the other miller indices.

$$i = -(h + k) \quad (3.1.3)$$

Given these known parameters, it is possible to correlate constructive interference patterns from X-ray diffraction to specific crystallographic planes. By matching combinations of diffraction signal peaks to their corresponding crystal planes, it is possible to identify crystalline materials and phases by X-ray diffraction peak intensity and pattern[26].

An XRD system typically consists of an X-ray beam source and a diffracted X-ray detector, with a stage on which powder or bulk samples are placed. Depending on the specific XRD system, either the beam source or the diffracted beam detector will rotate at an angle 2θ. If the crystal structure, including plane direction and lattice parameters, of a specific phase is known, it is possible the location of peaks by solving for θ from a combination of Bragg's Law using known lattice parameters.

$$2\theta = 2\sin^{-1}\frac{n\lambda\sqrt{h^2+k^2+l^2}}{2a} \quad (3.1.4)$$

Peak intensity and width can vary among samples of the same phase due to variations in grain size. A typical effect seen in XRD analysis is significantly broadened peaks in

samples with sub-micron grain sizes, which is typically explained through the Scherrer equation for powder diffraction.

$$\tau = \frac{K\lambda}{\beta \cos\theta} \quad (3.1.5)$$

where τ is the mean particle linear dimension, λ is the incident X-ray wavelength, β is the line broadening at half intensity, θ is the Bragg angle (previously calculated), and K is the unitless shape-factor, typically calculated to be approximately 0.93[27]. An amorphous material is typically expected to show a single, very wide curve, rather than a series of discrete peaks, due to the lack of any distinct crystal planes. Additional factors can also contribute to imperfections/irregularities in peak intensity, positioning, and width, including but not limited to improper sample preparation, misalignments/miscalibrations in the system, sample contamination, X-ray absorption, multiplicity, and the Lorentz-correction factor.

3.2 X-Ray Diffraction Analysis of Synthesized Powders

XRD analysis was performed as both a preliminary screening and a phase characterization technique on all synthesized and processed powders. Due to the synthesis and processing method, all samples were expected to include various polymorphs of SiO_2 in quantities greater than 5% by molar mass. All samples were prepared using the reverse-micelle/sol-gel process, and processed using matching heating rates and hold times, with only variations of temperature to attain the desired phase. A

heating rate of 150°C/hour with a hold time at temperature of 4 hours was used in thermal treatment of all samples. The processing temperatures used were 800°C, 900°C, 1025°C, 1075ºC, and 1100°C, which yielded samples with XRD peaks corresponding to γ-Fe_2O_3, a mixture of multiple Fe_2O_3 phases, ε-Fe_2O_3, a mixture of ε– and α– phases (potentially β–phase, and later confirmed with VSM), and α-Fe_2O_3, respectively (figure 3.2.1 and figure 3.2.2). Determination of crystal structure/phase composition was based on references from ICSD Database.

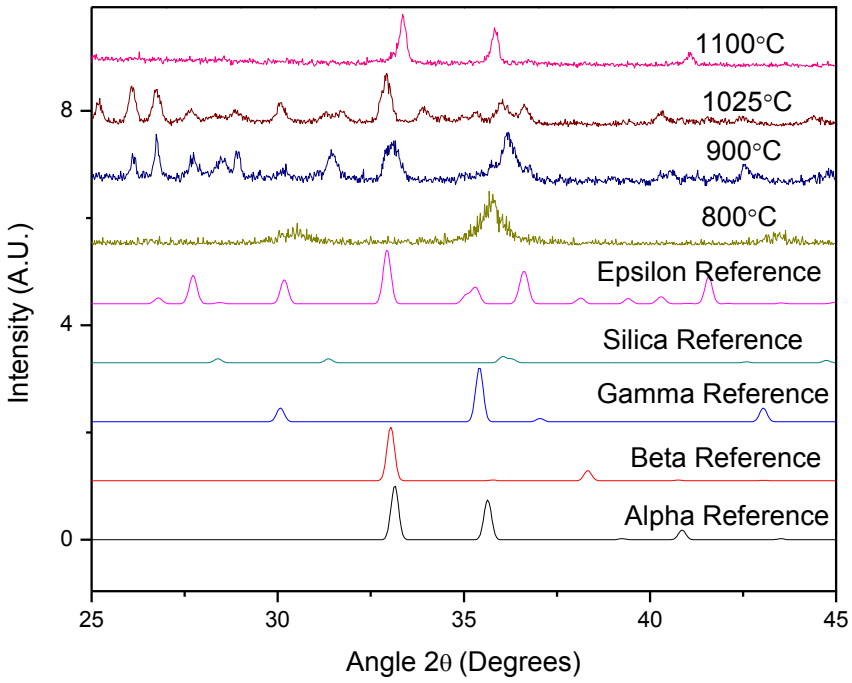

Figure 3.2.1 X-Ray Diffraction plot with varying calcination temperature

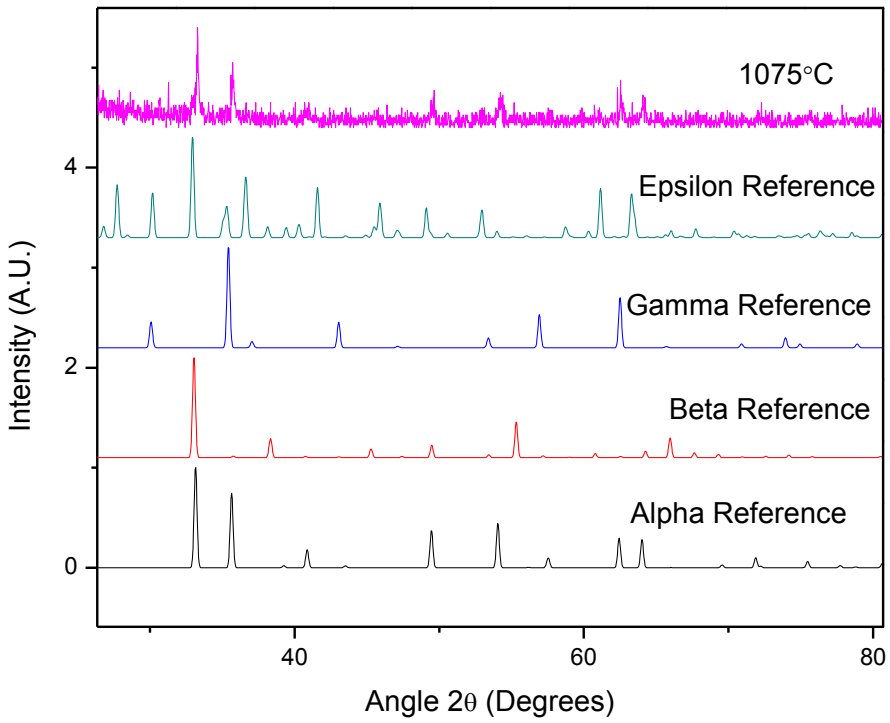

Figure 3.2.2 XRD Plot of synthesized powder calcined at 1075C

Initial XRD analysis showed a dominate cristobalite peak, a higher temperature polymorph of SiO_2, due to processing at 1100°C. Etching these earlier samples demonstrated distinct α-Fe_2O_3 peaks, likely due to processing conditions allowing for agglomeration of nanoparticles.

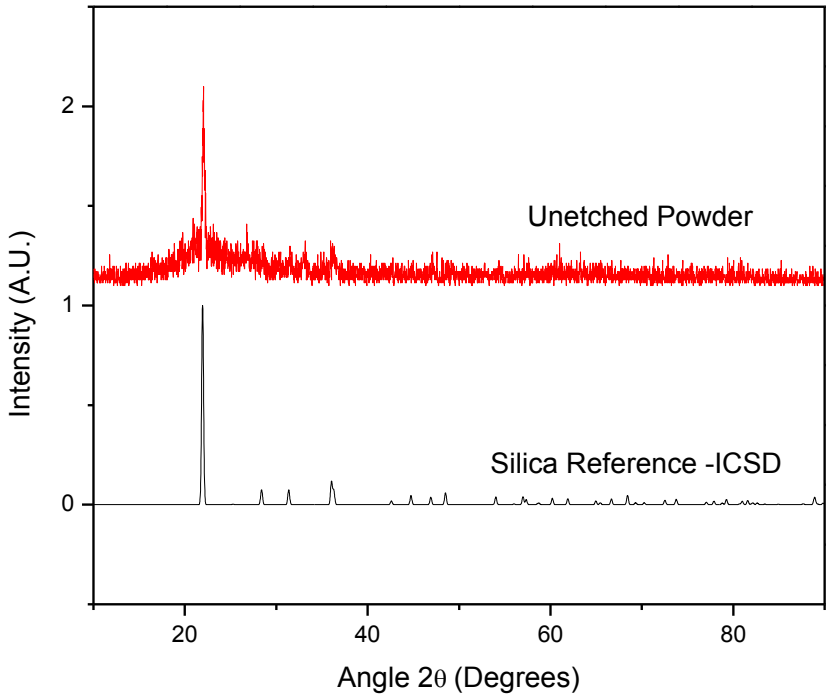

Figure 3.2.3 XRD of unetched powder sample showed primarily SiO_2 (cristobalite phase), with arbitrary normalized intensity units

Further processing of samples included variations in the hold temperatures and increased etching times to further remove the dominate SiO_2 peaks. The presence of α-Fe_2O_3 at lower-than-expected temperatures is attributed to the glass transition of the silica matrix above 1000° C, which allows for the agglomeration of individual particles.

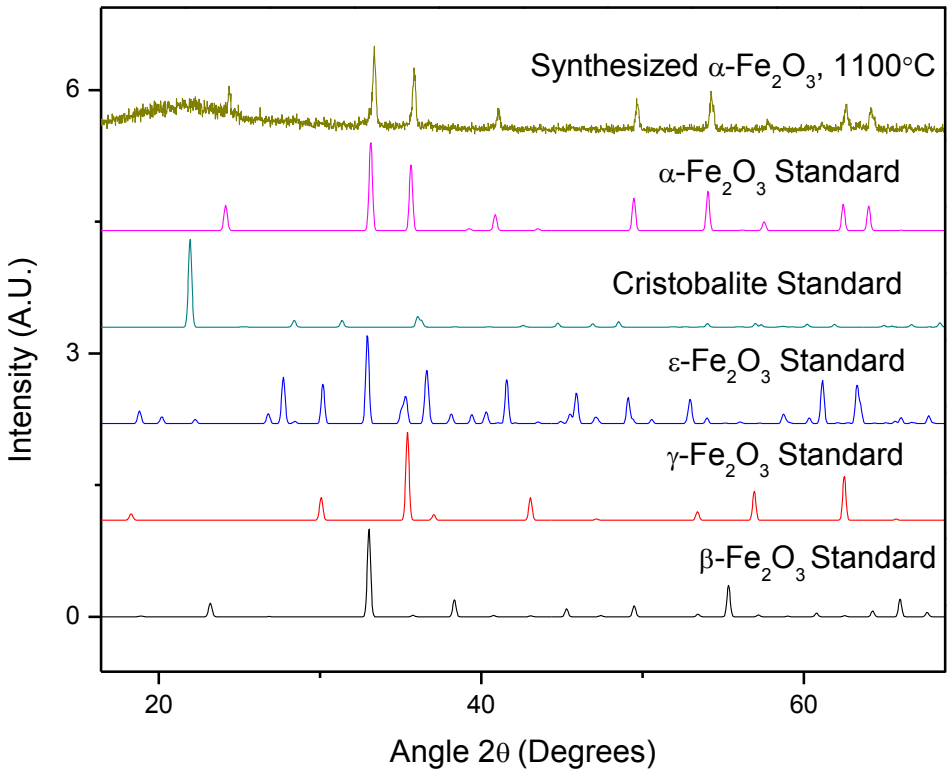

Figure 3.2.4 XRD of α-Fe_2O_3 becoming the dominant phase at sufficiently high calcination temperature (1100° C or higher), with arbitrary normalized intensity units

The as-synthesized powders were then processed at a lower temperature of 900° C, and displayed primary XRD peaks characteristic to both the γ- and α-phase (figure 3.2.3). This can likely be attributed to the agglomeration of nanoparticles prior to the silica matrix formation, leading to a direct transition from $Fe(OH_3)_3$ to γ-Fe_2O_3, then largely bypassing the predicted ε- and β-phases and transitioning directly into α-Fe_2O_3. Minor peaks that can be attributed to ε- and β- Fe_2O_3 appear to be present, but are largely overshadowed by the more dominant γ- and α-Fe_2O_3 peaks, due to the majority of

particles agglomerating and transitioning directly from γ-Fe_2O_3 to the most thermodynamically stable α-Fe_2O_3. A commercially purchased γ-Fe_2O_3 powder was used as a reference. A noticeable peak broadening is attributed to the significantly decreased grain size of between 20-60nm diameter.

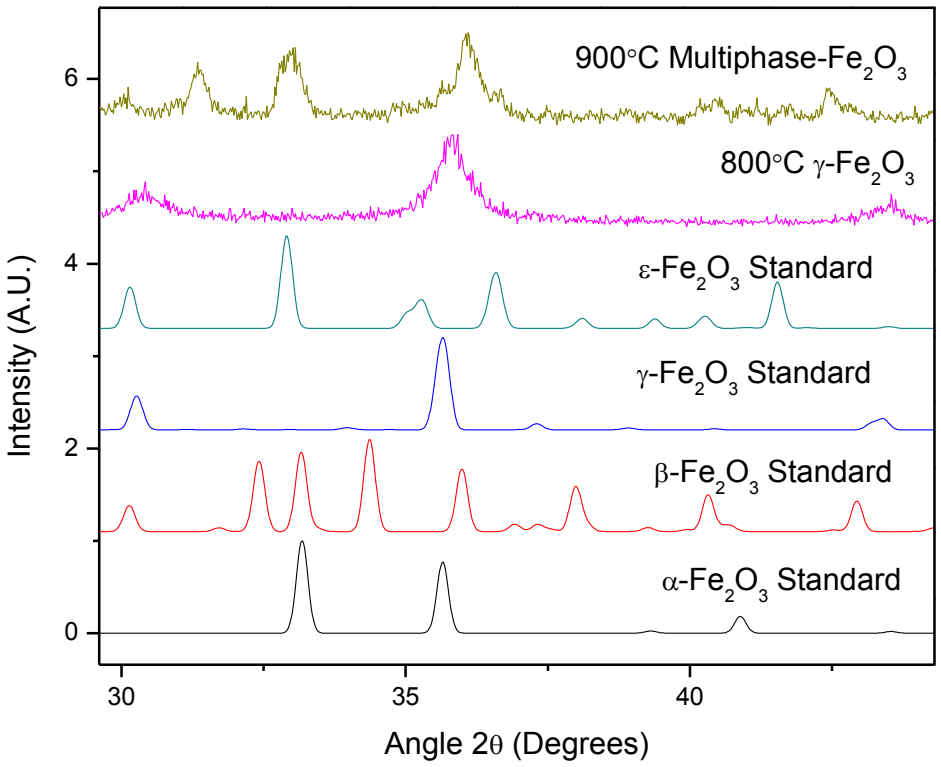

Figure 3.2.5 XRD peaks of a multi-phase sample showing peaks identified as both γ- and α-Fe_2O_3 phases, with additional unidentified minor peaks, with arbitrary normalized intensity units

These powders were then calcined at 1025° C for 4 hours and the silica matrix was etched for 2 hours. XRD analysis showed a series of peaks that correspond primarily with ε-

Fe_2O_3, although the continued presence of a cristobalite shell reduced the overall intensity of the ε-phase peaks (figure 3.2.5 and 3.2.6).

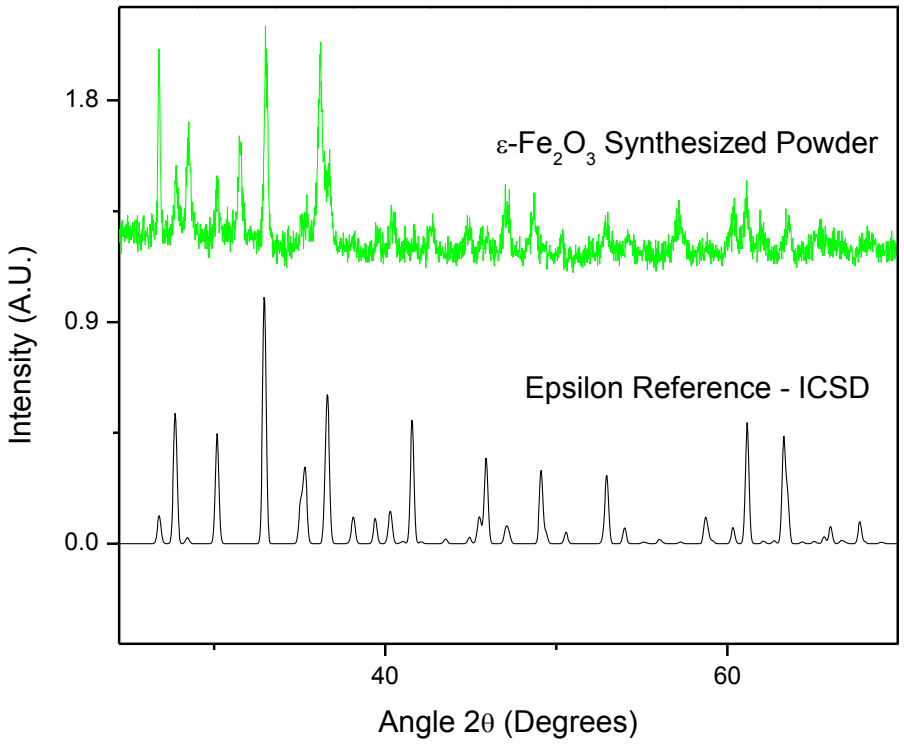

Figure 3.2.6 XRD of synthesized ε-Fe_2O_3 powder compared directly with standard reference XRD plot, with arbitrary normalized intensity units

A normalized-intensity and expanded view of multiple ε-Fe_2O_3 samples revealed a close match to the diffraction peaks of the ε-phase standard.

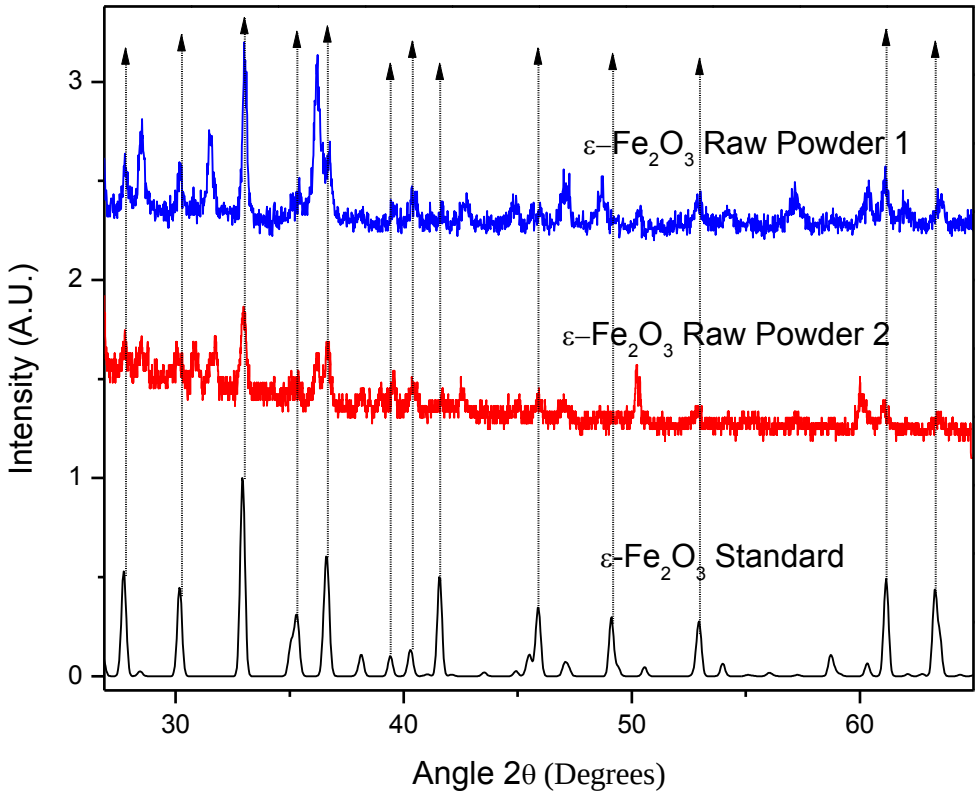

Figure 3.2.7 XRD plot of multiple ε-Fe_2O_3 powders with peaks matched to ε-Fe_2O_3 ICSD reference

Throughout all XRD analysis, a crystalline silicon powder was used as a reference powder in order to ascertain potential peak position or intensity shifting due to non-powder related conditions, such as miscalibration of the system.

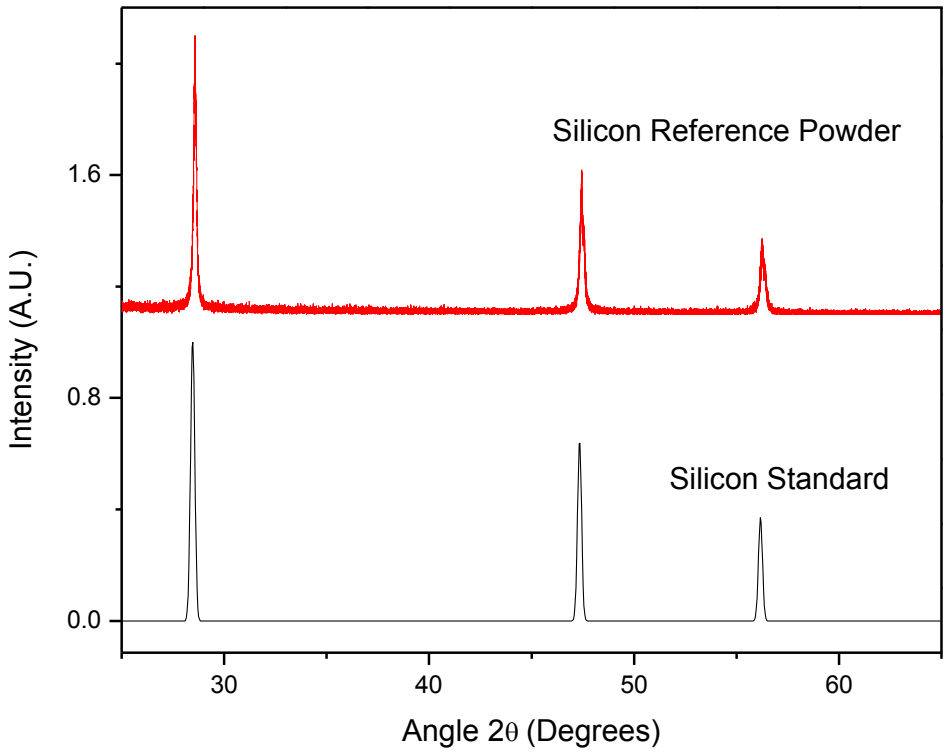

Figure 3.2.8 XRD comparison of silicon reference powder to silicon standard, used to as an equipment check

X-Ray Diffraction was used as a preliminary characterization tool to identify potentially desirable phases for various magnetic applications. With XRD as a screening method, it was possible to determine specific synthesis and processing conditions necessary to attain the desired crystal structures of Iron (III) oxide.

3.3 Background on Scanning Electron Microscopy

While X-ray Diffraction is a useful characterization tool for determining crystal structure and phase, in the case of magnetic materials, morphology, or shape of a grain, is also important. As explained in a previous section, the behavior of permanent magnetism in materials is heavily dependent on the influence of multiple magnetic domains size and orientation with respect to each other. To determine morphology and grain size, it is often useful to have visual confirmation. However, due to the typical human eye being unable to resolve below the micron level with a standard optical microscope, other means must be used. Because of its ease of use and relatively high accuracy, Scanning Electron Microscopy (SEM) is an often-used tool for surface morphology and grain size characterization of both powder and bulk samples above 10nm and up to several hundred microns.

In Scanning Electron Microscopy, an electron beam is typically generated either by thermionic electron emission, or field electron emission. Thermionic electron emission guns are comprised of both a cathode and an anode, with a filament (usually tungsten or lanthanum hexaboride) acting as the cathode, is heated to the point which electrons are energized to the point where they are able to overcome the work function energy of a material, and escape into a vacuum toward the anode. The current density of thermionic emissions from such a cathode is described by the Richardson equation[28].

$$J_c = A_c T^2 \exp\left(-\frac{E_w}{kT}\right) \quad (3.3.1)$$

Where J_c is the current density, A_c is the constant value 120 A/cm^{2}K^2 for thermionic emitters, T is temperature, k is the Boltzmann constant, and E_w is the work function energy. In a field-emission electron gun, an electric field is applied to a solid material acting as a cathode which then ejects electrons through multiple anodes into a vacuum. The resolution of an image generated in scanning electron microscopy is partially dependent on the brightness (B) of the electron beam.

$$B = \frac{4I_b}{(4d\alpha)^2} \quad (3.3.2)$$

Where I_b is the beam current, d is the beam diameter, and α is the beam convergence or divergence angle.

To attain sufficient energy for microscopy purposes, emitted electrons must be accelerated by an excitation voltage. At sufficiently high velocities, (and considering it a particle) an accelerated electron begins to behave in a relativistic manner, in which its mass begins to increase compared to its rest mass.

$$m = \frac{m_r}{\sqrt{1-(\frac{v}{c})^2}} \quad (3.3.3)$$

Where m_r is the rest mass of the electron, v is the velocity, and c is the speed of light ($3.0x10^8$ m/s^2). However, due to the wave-particle duality nature of electrons, the DeBroglie relation must be considered, in which the wavelength of an electron-wave is dependent on its velocity[28].

$$\lambda = \frac{h}{p} = \frac{h}{m_r v} \quad (3.3.4)$$

In DeBroglie's equation, λ is the electron wavelength, which is dependent on Planck's constant ($h = 4.1357 \times 10^{-15}$ eVs) and the particles momentum ($p = m_r v$), where m_r is the particle rest mass and v is the particle velocity. Further relating the relativistic change in mass to the DeBroglie wavelength equation, the wavelength of a relativistic electron is shown to be

$$\lambda = \frac{h}{\sqrt{2eVm_r + (\frac{eV}{c})^2}} \quad (3.3.5)$$

where eV is the energy in electronvolts.

After being accelerated to sufficient velocities, an electron beam must be focused. In a manner analogous to optical microscopes, the electron beam passes through a series of electromagnetic "lenses". These lenses are typically solenoids, which generate a magnetic field, exerting a Lorentz force on an electron equivalent to

$$\vec{F} = q(\vec{V} \times \vec{B}) \quad (3.3.6)$$

where q is the particle charge, V is the velocity vector and B is the magnetic field vector. A typical SEM system is comprised of one to three condenser lenses, which serve to demagnify the electron beam, or adjust the spot size. The final lens in the series is the objective lens, which serves to adjust the actual focus of the image by altering the current flow going through the lens[29].

In SEM, due to the energetic behavior of electrons, multiple emissions can be generated from an electron beam interacting with a sample, including unscattered electrons, inelastically scattered electrons, elastically scattered electrons, absorbed electrons, backscattered electrons, secondary electrons, X-rays, Auger electrons, and light (UV, visible, or infrared). Under most circumstances, SEM detectors utilize either secondary electrons or backscattered electrons to generate bright-field or dark-field images, respectively. The emitted X-rays of sufficiently high energy (typically requiring an acceleration voltage of 20kV) can also be used for elemental analysis of samples in a process known as Energy-Dispersive Spectrometry (EDS)[28].

3.4 Scanning Electron Microscopy of Synthesized Powders

SEM was performed on synthesized powders at various stages of the synthesis process, ranging the pre-calcination powder to the fully formed and etched nanorod samples. All SEM imaging was conducted with excitation voltages ranging from 10-20kV, and were synthesized using the same chemical processes but with altered mixing times to compensate for various powder requirements. To acquire SEM images, samples must be conducting, coated with a conducting material, or scanned with low-energy (low excitation voltage) electrons, otherwise absorption of highly energetic electrons causes surface charging, which greatly distorts image quality. Because both SiO_2 and Fe_2O_3 are non-conducting materials, initial attempts at SEM analysis for morphology yielded poor resolution images and inconclusive results. Subsequent samples were sputter-coated with

a thin layer of platinum/palladium, a conductive layer to prevent surface charging of samples.

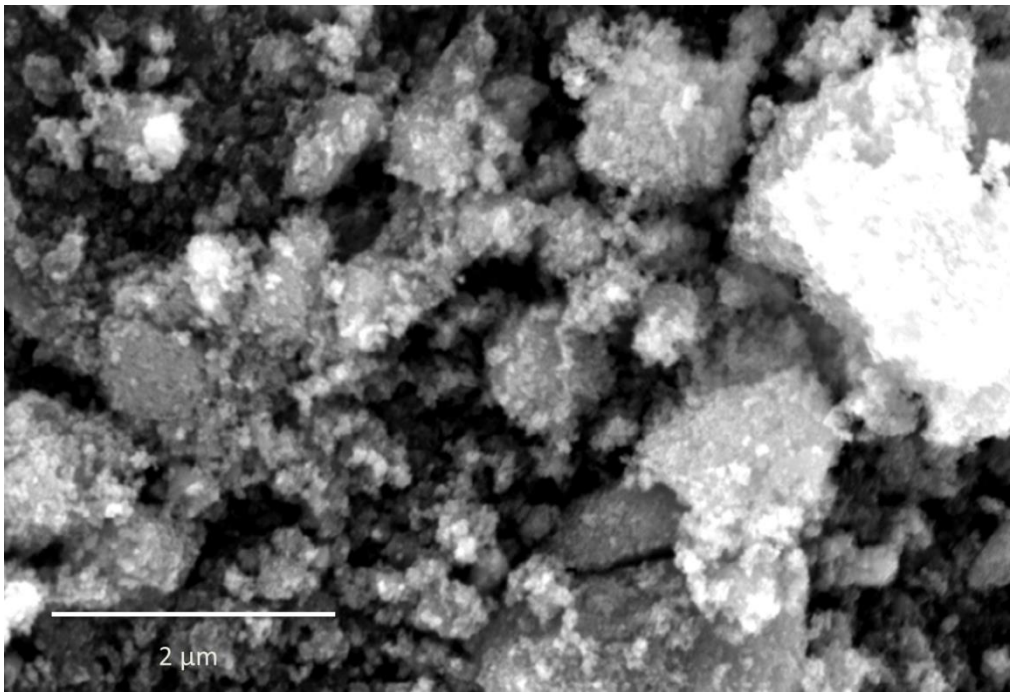

Figure 3.4.1 SEM micrograph of powder calcined at 600°C without Pt/Pd sputter coating showed large amounts of surface charging, limiting the ability to resolve small features

Samples imaged prior to calcination showed clusters of large, irregularly shaped particles. It was predicted that the iron hydroxide particles would be below the resolution limit of the SEM due to the small (10nm or smaller) grain sizes. Furthermore, because the powder was both uncalcined and unetched, the silica was predicted to have remained in an amorphous phase, as well as being the only SEM-resolvable component in the powders. EDS analysis showed a large presence of elemental silicon and oxygen, with

trace amounts of iron and carbon (figure 3.4.2). The presence of carbon in the sample is attributed to the use of carbon tape in preparing powder samples for SEM analysis.

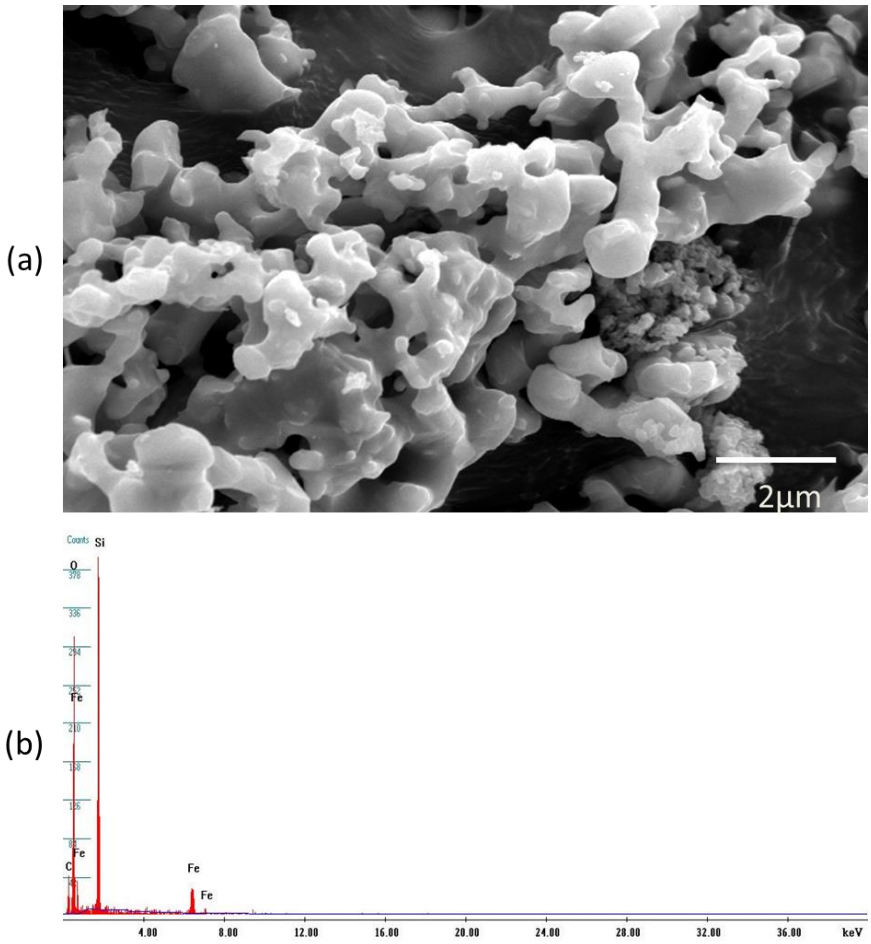

Figure 3.4.2 (a) SEM micrograph and (b) EDS analysis of pre-calcination powders

Calcination at 1000° C with partial KOH etching of the silica matrix showed the early stages of nanorod formation (figure 3.4.3). The majority of nanorods were randomly distributed and partially coated by the silica matrix. Samples processed at this

temperature demonstrated nanorods uniformly around 100nm in length, and widths of approximately 20nm.

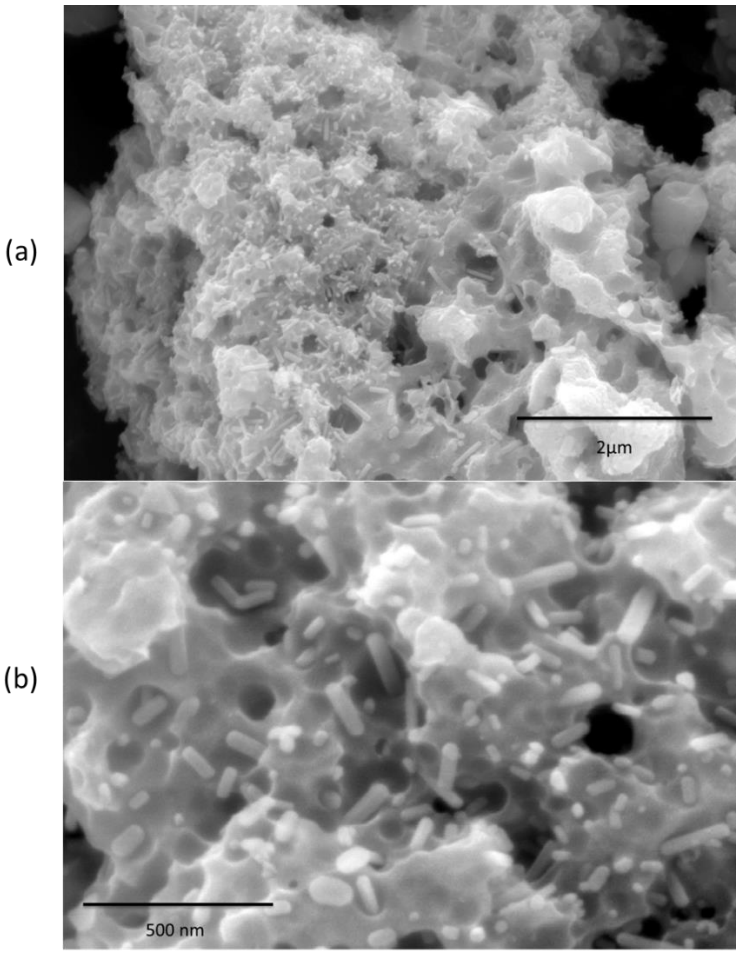

Figure 3.4.3 SEM micrograph of powder calcined at 1025°C and KOH-etched at (a) low magnification and (b) higher magnification

Higher magnification imaging showed that the nanorods formed were uniformly within the 100nm length range, and protruded from the silica matrix with varying orientations.

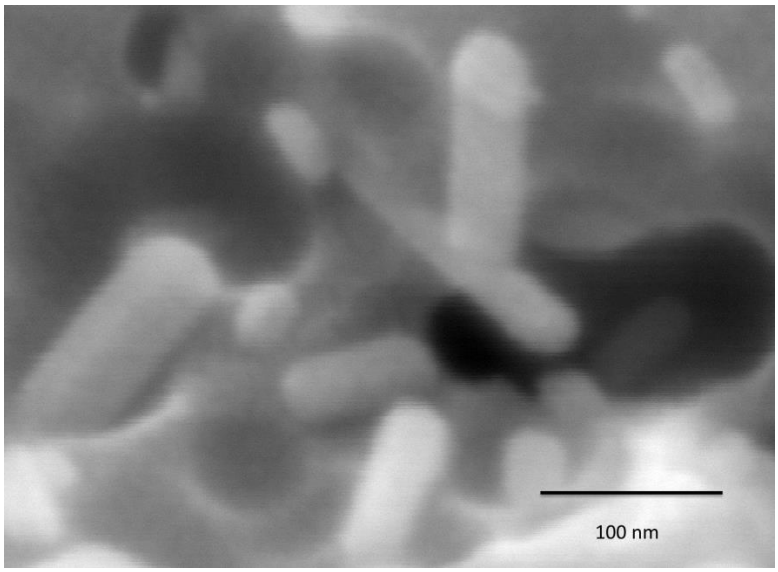

Figure 3.4.4 SEM with higher magnification view of nanorods show a uniform approximate length of 100nm

Later samples were processed at higher temperatures ranging from 1025°C - 1100°C, and with improved dispersion of alkali ions during the synthesis process. These samples were then etched at higher temperatures but with decreased etching times to pinpoint the desired amount of silica. SEM analysis showed a greater aspect ratio in the nanorods formed. Typical nanorod lengths ranged from 300nm to over 500nm, with typical widths remaining in the 20-30nm range.

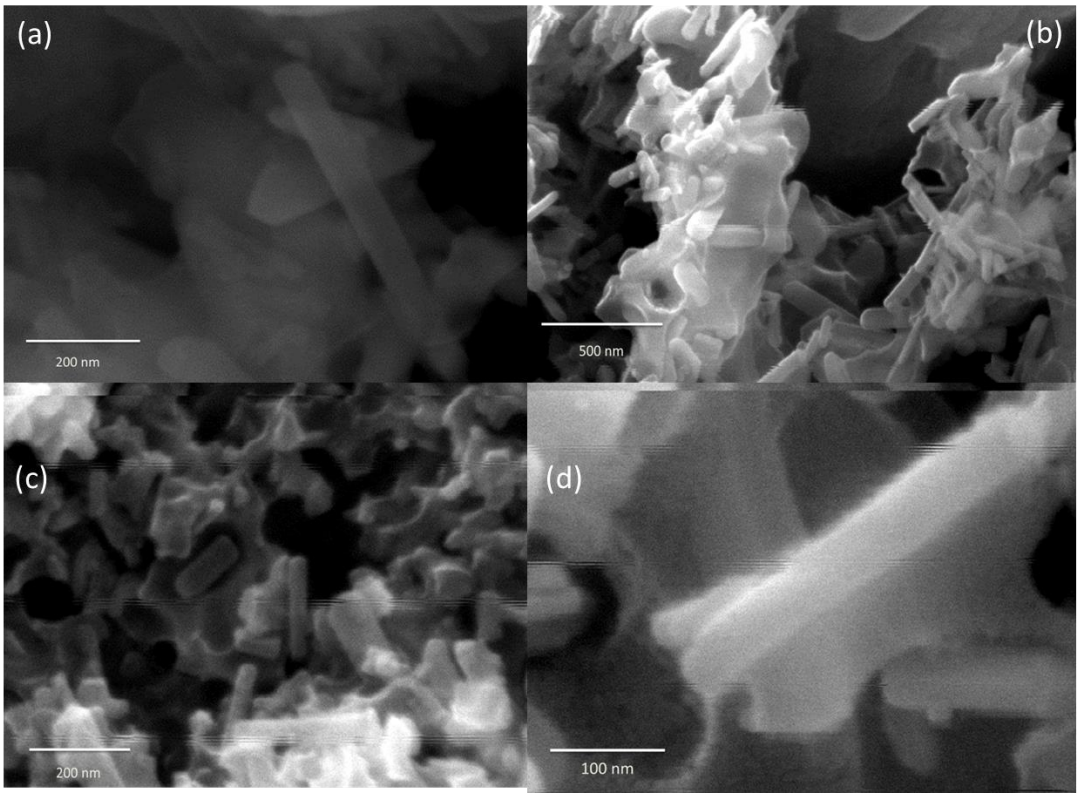

Figure 3.4.5 SEM micrograph of powder calcined at 1025°C and etched with KOH at various magnifications, demonstrating average nanorods length of 300-500nm

SEM analysis of samples processed at varying conditions showed that the morphology of the powder was dependent on both the initial synthesis process as well as the processing time and temperature. In general, a combination of longer calcination times and higher temperatures allowed for nanorod formation.

3.5 Background on Vibrating Sample Magnetometry

When characterizing a permanent magnetic material, it is often most useful to obtain a hysteresis relating applied field to magnetic moment (M vs H curves). A Vibrating Sample Magnetometry (VSM) system offers the unique advantage of a fast and accurate general-purpose method of magnetic hysteresis characterization while naturally filtering any external magnetic field contributions. A VSM relies on Faraday's principals of electromagnetic induction to produce a potential difference through a changing magnetic field which is then correlated to the magnetic moment of the sample.

The design of a VSM system is fairly simple, comprised of a vibrating sample head, used for oscillating a magnetic sample perpendicular to the magnetic field generated by two toroid electromagnets. The field generated by the electromagnets is typically directed to a central location with high-magnetic permeability pole pieces. Mounted on these pole pieces are pickup coils, which generate an electromotive force, or a bias voltage, when in the presence of a changing magnetic field, as explained by Faraday's Law of Induction equation[30].

$$\varepsilon = -N\frac{d\Phi_B}{dt} \quad (3.5.1)$$

Where ε is the generated electromotive force, or voltage, N is the number of turns in a tightly-wound coil, Φ_B is the magnetic flux, and t is the time. Similarly, the Maxwell-Faraday equation further expands upon this concept by introducing the space-varying electric field related to the time-changing magnetic field[31].

$$\nabla \times E = -\frac{dB}{dt} \quad (3.5.2)$$

Where ∇ is the curl operator, E is the electric field that is generated, B is the magnetic field, and t is the time.

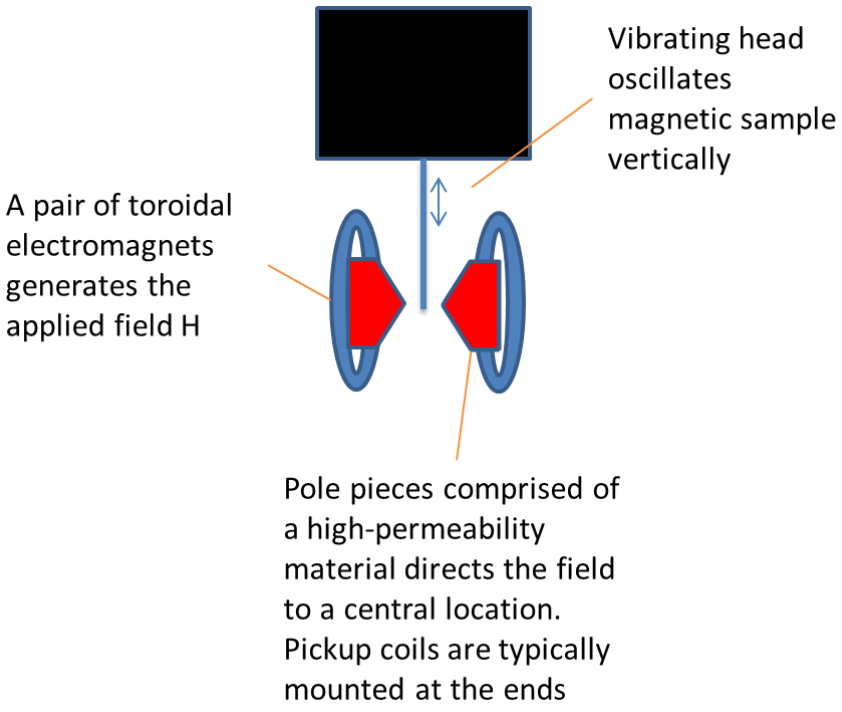

Figure 3.5.1 Simple diagram of a VSM system containing two pole pieces and electromagnets on each side of a sample oscillated by a vibrating head

Using the applied field to magnetize the sample, the changing field produced by the sinusoidally vibrating sample then induces a changing voltage. The voltage is then correlated to the magnetic moment of the material, and can be used to obtain a hysteresis curve plotting the materials magnetic moment (M) in relation to the externally applied field from the electromagnet (H). A magnetic hysteresis curve is useful in identifying

permanent magnetic behavior of a material due to the information that can be obtained, including the initial magnetization curve, saturation magnetization, remanence, coercivity, and any shifting of the curve.

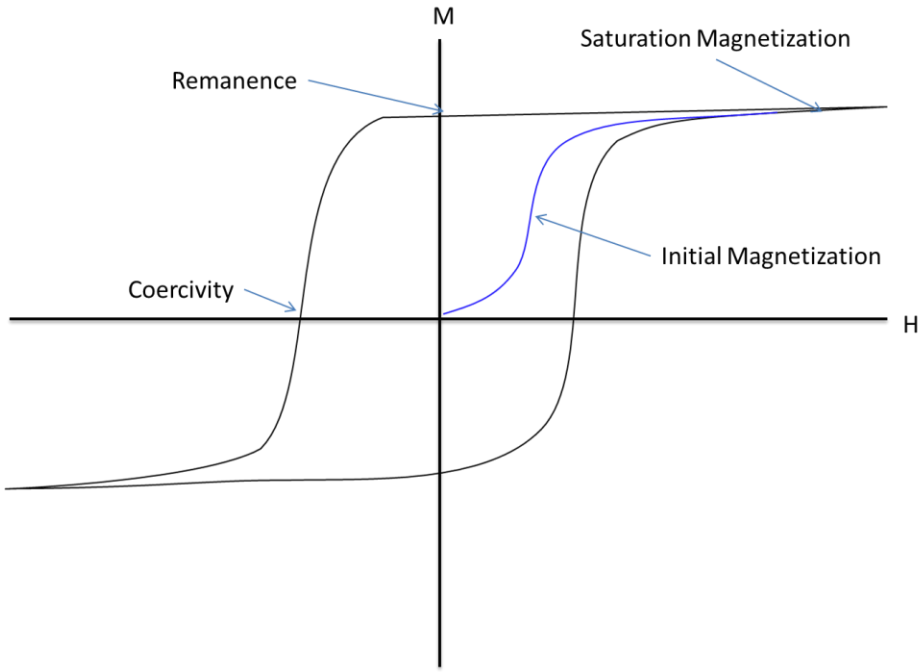

Figure 3.5.2 Diagram of various aspects of magnetic hysteresis curve, with applied field (H) on the x-axis and magnetic moment (M) on the y-axis

Initial magnetization of the sample can provide valuable information on the interaction of the domains within the sample. For example, if the initial magnetization curve has a very steep slope, then it is likely the magnetic domains in the material readily change direction to align with an external field (i.e. paramagnetic materials tend to be linear), whereas if the slope is non-linear and has shallow, changing slopes throughout, then it can be assumed that the magnetic moments may be arranged in such a way as to

oppose external magnetization effects. Furthermore, diamagnetic materials will respond in a way that directly opposes the applied magnetic field, and the initial magnetization curve would show an increasing magnetic moment inversely proportional to the applied field. Under sufficiently high applied fields, ferri-, ferro-, and certain canted-antiferromagnets reach a point of maximum magnetization, at which point all magnetic moments within the materially are completely aligned in the direction of the applied field. Materials which can be permanently magnetized will tend to reach a point where the slope of the magnetic moment becomes flat, or nearly flat, indicating the point of saturation. Once at the saturation point, if the direction of the applied field is reversed, the slope of the magnetic moment can provide further evidence of the type of magnetic material. A paramagnetic material will continue to have a changing magnetization that is linearly proportional to the applied field, whereas a material that can be permanently magnetized will display a hysteretic behavior.

At the point where there is zero applied field, a permanent magnetic material will retain a certain amount of the initial magnetization, known as the magnetic remanence. The remanence of a material is a further indicator of how readily magnetic domains in a material align to an applied field and respond magnetically. Following the zero-field point, the external magnetic field then proceeds to flip direction, and begins to apply a field to the material directly opposite that of the initial magnetization curve. With a field applied in opposition to the initial magnetization, the magnetic domains within a permanently magnetic material will initially resist changing direction. When the opposite-direction field is of sufficiently high magnitude, the magnetic moments in the

material will begin to flip to align with the external field. The point at which the magnetic moment of the material returns to zero is known as the coercivity. Coercivity of a material is a strong indicator of the "hardness" of a magnet, or how well a material is able to retain its magnetization. The coercivity and remanence of a material can be used to obtain a value known as the energy product, or BH_{max}, which is the largest rectangular area that can be calculated to fit within the hysteresis curve in the negative field/positive magnetization quadrant, and is an indicator of how strong a permanent magnet is overall[4], [32]. Typically, a "soft" permanent magnet will have high magnetic remanence, due to the ability to align completely with an external magnetic field, and thus display an extremely tall and narrow hysteresis curve. Meanwhile, a "hard" magnetic material display a large coercivity, but not necessarily a high remanence, and therefore the hysteresis for such materials tends to be very wide and short. An ideal permanent magnet would display both high remanence and coercivity, and fit the theoretical shape of a magnetic hysteresis.

3.6 VSM Measurements of Synthesized and Calcined Powders

The various Fe_2O_3 phases were magnetically characterized using a Lakeshore 7400 series VSM. All processes were performed using synthesized α-Fe_2O_3 powder, calcined at 1100°C, as a reference material, with the phase confirmed through XRD analysis. Due to limitations of the system, a maximum of 17.5 kOe applied field was used. γ-Fe_2O_3 is a ferrimagnetic phase, and considered a soft magnet. A high remanence

with low coercivity was expected. α-Fe_2O_3 is an antiferromagnet, and expected to be unsaturated, with low remanence and coercivity. β-Fe_2O_3 is a paramagnetic phase, and would display neither remanence nor coercivity, due to the tendency of paramagnetic materials to randomly reorient after an applied field is removed. ε- Fe_2O_3 is a canted antiferromagnet, and predicted to display an extremely high coercivity with low remanence, and to be unsaturated at fields below 50 kOe. Samples processed at 900°C displayed magnetic properties indicative of a mixture of multiple phases of both ferrimagnetic and anti-ferromagnetic phases.

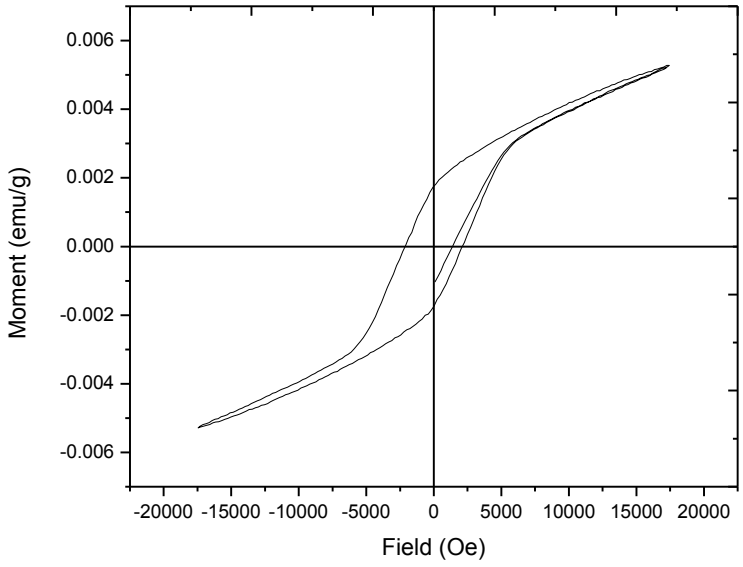

Figure 3.6.1 Hysteresis loop of powder samples calcined at 900°C showing a relatively high remanence and coercivity, reminiscent of both ferrimagnetic, and canted-antiferromagnetic phases

The initial magnetization curve of these earlier samples showed a steep two-segment linear response, along with an inability to full saturate, indicating a combination of paramagnetic and antiferromagnetic phases. The low remanence and fairly high coercivity indicated the potential for a hard magnetic phase. Additionally, the noticeable left shift is typically an indicator of an exchange bias between two or more different types of magnetic materials[33]. SEM analysis of these samples indicated the early stages of nanorod formation, and XRD analysis confirmed the presence of multiple phases.

Subsequent samples were processed to obtain the desired nanorod morphology as well as crystal phase isolation by calcining at 1025°C. In samples displaying distinct nanorods, XRD analysis indicated a majority of ε-phase, with VSM data confirming magnetic behavior expected of a canted-antiferromagnetic material.

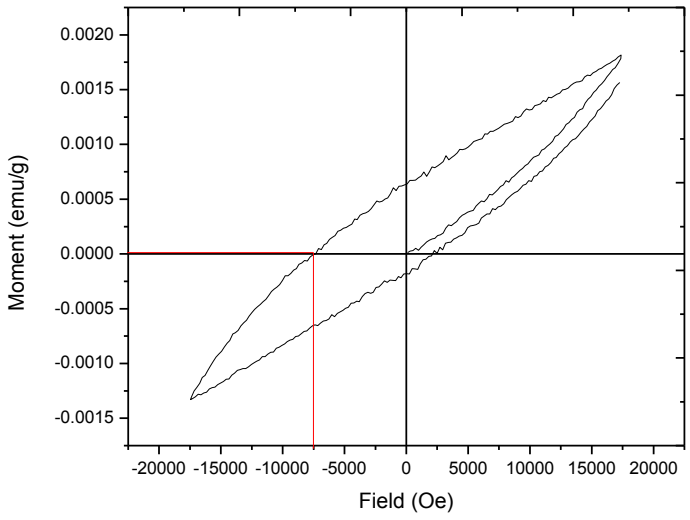

Figure 3.6.2 Hysteresis loop of ε-Phase samples processed at 1025°C with high coercivity and extreme left-shifting[14]

Further refinement of the powder synthesis method by altering mixing times to obtain higher aspect-ratio nanorods were shown to retain the majority ε-phase composition, and demonstrated significantly higher coercivity. In addition to the significantly larger coercivity, the lack of saturation was more pronounced, with the slope increasing rather than decreasing, and a noticeably open hysteresis loop. An increased remanence as well as a more pronounced left-shift of the hysteresis indicates either a potential exchange coupling, or the influence of multiple, differing magnetic domains in an organized sequence (i.e. arranged throughout a nanorod)

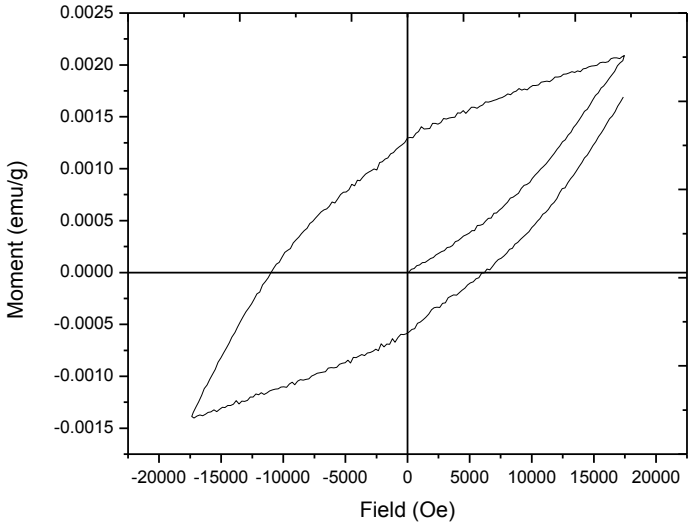

Figure 3.6.3 Hysteresis loop of ε-Fe_2O_3 powder after refinement of synthesis and processing methods yielded higher aspect-ratio nanorods demonstrated significantly higher (non-saturation) coercivity

Samples demonstrating a primarily paramagnetic behavior were also through calcination at 1075ºC. As-synthesized samples demonstrated a primarily linear hysteresis, without a

saturation magnetization, and a slight left-shift, indicating a majority paramagnetic phase coupled with potentially antiferromagnetic phase, as would be expected in a β-phase to α-phase transition point.

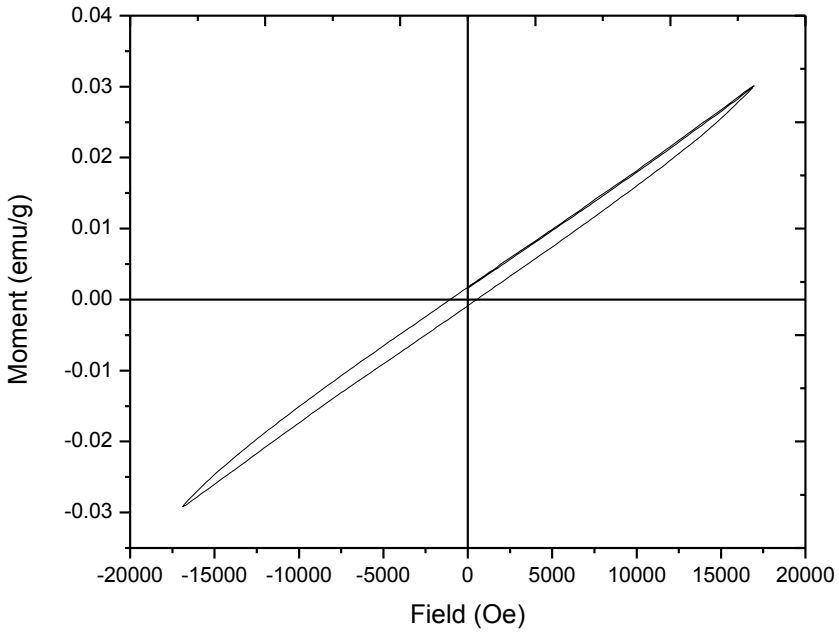

Figure 3.6.4 VSM of powder calcined at 1075ºC

The antiferromagnetic α-phase was also identified using XRD, and characterized with VSM. A low coercivity and remanence and an inability to saturate was demonstrated, as expected of antiferromagnetic materials. The antiferromagnetic α-phase powder was synthesized through calcination at 1100°C, and used as a reference powder throughout each separate series of VSM measurements as a reference. In doing so, the consistency of

system calibrations was confirmed, along with elimination of external influences on the results.

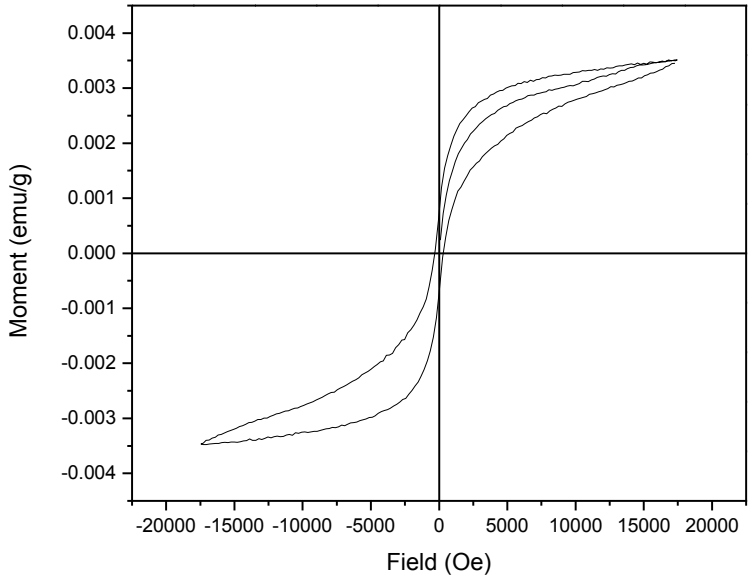

Figure 3.6.5 Hysteresis of α-Fe_2O_3 reference powder, to verify VSM equipment consistency

Additional VSM analysis was performed on synthesized pure silica samples. As expected, the dominant magnetic characteristic demonstrated in such samples was the diamagnetic nature of silica.

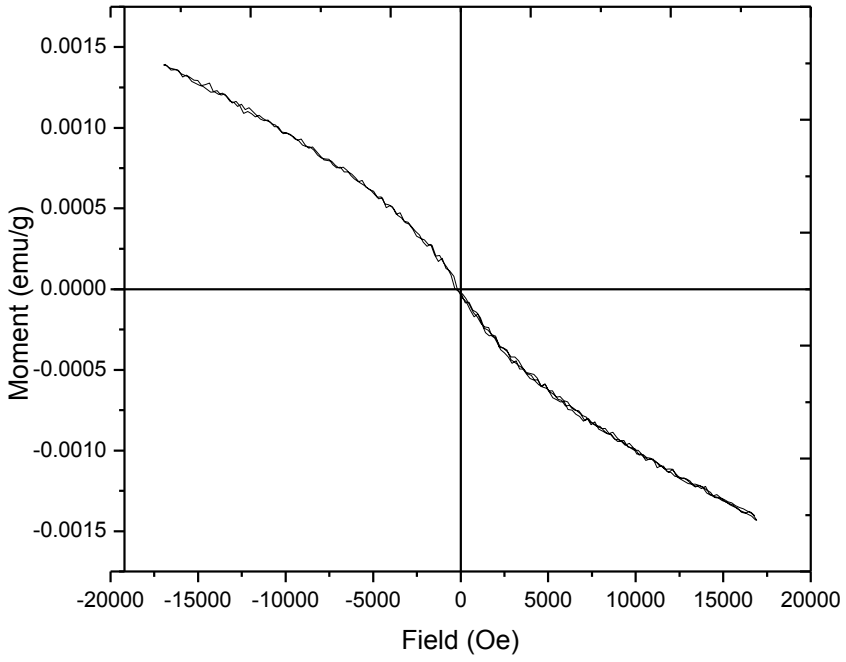

Figure 3.6.6 Hysteresis loop of diamagnetic (negative moment response to increasing external magnetic field) behavior of the silica matrix is dominant in unetched samples

Through the use of VSM characterization, various phases of Fe_2O_3 were characterized. Each phase demonstrated magnetic behavior expected of ferrimagnetic, paramagnetic, antiferromagnetic, and canted-antiferromagnetic materials, with coercivity, remanence values, varying applied fields necessary for full saturation, and initial magnetization curves which were useful for interpreting interaction between the magnetic domains within the material.

Chapter 4 – Densification of Powders through CAPAD Process and Characterization of Iron Oxide/Silica Composite Structures

4.1 Overview of CAPAD:

Current Activated Pressured Assisted Densifcation (CAPAD) is a process which relies on a high current to induce Joule heating while simultaneously applying a load pressure to allow for rapid sintering of powders. Densification of powders is a function dependent on both thermodynamics and kinetics, and thus temperature, time, and pressure are the primary parameters to be considered in attaining high density (greater than 95% pore-free). By utilizing rapid joule heating (at heating rates ranging from 200º - 600º C/minute) to reach densification temperatures while simultaneously applying a load pressure (typically in the range of 50 – 100 MPa, and at times as high as 500 MPa), it is possible to attain full density (95-99% density) in minutes rather than the several hours necessary in traditional sintering processes[11].

The advantages of densifying materials through CAPAD are especially evident when dealing with optical materials and intermediate/metastable phases. Typically, optical materials require high density and purity, with even trace amounts of pores, imperfections, and dopants/inclusions acting as photon scattering sites. While unwanted doping or inclusions must be erradicated at the powder preparation level, the ability to reach fully density in minimal time through CAPAD processing allows for the simultaneous elimination of unwanted porosity while preserving grain size and structure, thereby creating ideal optical materials[11]. A further consequence and advantage of

CAPAD processing is the ability to control and overcome the thermodynamic instability, or the preservation of metastable phases. Typically, metastable phases cannot exist under normal (non-rapid CAPAD processing) processing conditions due to the time and temperature dependence of material phases[7]. However, with the rapid Joule heating and high load pressure, it is possible to preserve metastable phases in bulk forms.

4.2 CAPAD System and Sample Preparation

The CAPAD system used in all powder processing consisted of two copper electrodes with graphite spacers acting as the actual heating and pressure contact on the samples. Load forces of up to 600kN are applied by an Instron 5500 series load cell. The graphite spacers and samples are enclosed within a water-cooled vacuum chamber to prevent oxidation reactions during processing. Typical experiments were conducted with temperature monitoring through either a thermocouple (at 1200º C or below) or a pyrometer (above 1200º C).

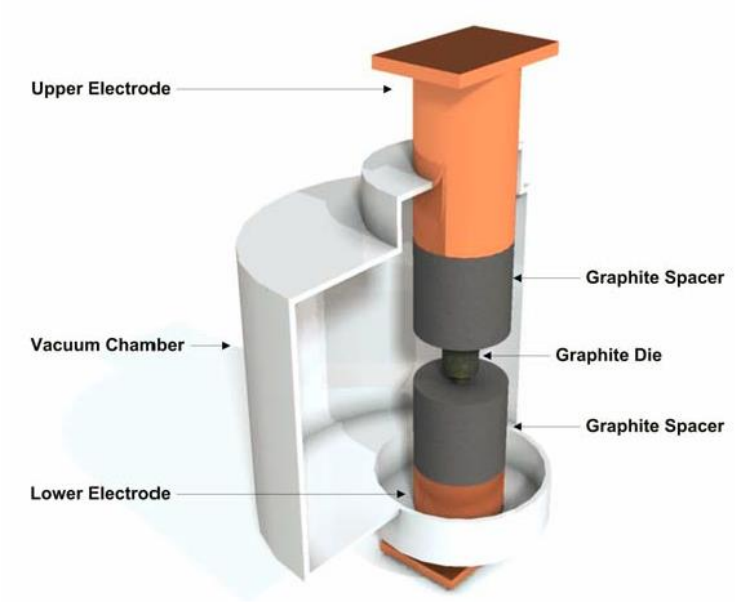

Figure 4.2.1 Schematic of CAPAD System, in which powder is pressed within a graphite die and plunger set, and a combination of rapid joule heating through copper electrodes and high pressure are applied simultaneously to rapidly densify powders [14]

Sample powders were prepared using a two-part graphite die/plunger setup. In order to minimize powder usage and to increase homogeneity of densified samples, 0.17-0.20 g of powder was placed within a pre-broken miniature graphite die of 5mm inner diameter and 20mm outter diameter, and pressed between two 10mm miniature plungers. The smaller die and plunger set was then inserted into a larger graphite die with 20mm inner diameter, and pressed between two larger 20mm diameter diffuser plungers.

4.3 Densification and Density Measurements of Core-Shell Samples

All CAPAD-processed powders were synthesized through the reverse-micelle/core-shell process, with iron oxide concentrations ranging from 0.0, 0.01, 0.5, 1.0, and 2.5 mol%, and a pure silica powder prepared without reverse-micelle structures as a reference powder with minimal organic contamination. Using the 10mm miniature system, 0.17-0.18g of each powder was insert into the die and plunger sets, and prepressed with a ramp rate of 2.0kN/min up to 7.1kN, holding for 2 minutes, then released at a rate of -2.0kN/min back to 0kN. The samples then densified with a load rate of 2.0kN/min and simultaneously heated at an approximate rate of 100ºC/min up to 380ºC. Upon reaching the desired 7.1kN processing load (100MPa),the sample was then further heated at a rate of 200-250ºC/min up to the desired temperature and held at temperature for five minutes. Three temperatures of 900ºC, 1050ºC, and 1100ºC were used for the study, based on the transparency range of synthesized silica powders. Discernable transparency for visible light wavelengths (approximately 450-700nm) was appearant in silica-only samples processed at 900ºC and above. Below 900ºC, samples were opaque and completely white. Following CAPAD processing of samples, load pressures of approximately 5.0kN were maintained in order to facilitate active cooling, in effect quenching the processed samples and lowering the die temperature down to 25ºC or lower within 15 minutes.

Theoretical densities were calculated through a simple rule of mixtures, based on the assumption of a two-phase composite.

$$Density = (Density\ A\ \ \%ConcentrationA) + (Density\ B\ \times \%ConcentrationB)$$

Due to the low iron oxide concentrations, characterization of the iron/iron oxide phase was below the resolution capabilities of X-Ray Diffraction. Therefore, the highest and lowest theoretical densities were used for comparison of samples to determine approximate relative density values. The highest theoretical density was assumed to be the case of a iron oxide-reducing atmosphere in which magnetite (Fe_3O_4) is formed, and tridymite, a low density silica polymorph typically formed above 870ºC, forms the external shell structure. A lowest theoretical density was calculated assuming the formation of the most stable iron (III) oxide polymorph, hematite (α-Fe_2O_3) in a composite with α-quartz, a common lower-temperature silica polymorph. While a higher density polymorphs of silica exists in the form of coesite and stishovite, the formation of such phases is unlikely due to the extremely high pressure conditions necessary for formation (greater than 20GPa)[34], [35].

mol% Iron Oxide	Lowest Theoretical Density	Highest Theoretical Density
0	2.28	2.65
0.01	2.280272	2.65026
0.5	2.2936	2.663
1	2.2805	2.676
2.5	2.348	2.715

Table 4.3.1 Lowest and highest theoretical densities for varying iron oxide concentrations ranging from 0.0 to 2.5 mol%

The maximum iron oxide concentration which exhibited high optical transparency was 0.5 mol%, and was the primary focus of subsequent characterization and studies, with synthesized silica studied in conjunction as a baseline comparison. Subsequent XRD characterization of synthesized samples, as expected, showed that the iron oxide concentrations were well below the detection limits of typical XRD systems, and that α-quartz was the dominant silica phase in transparent samples.

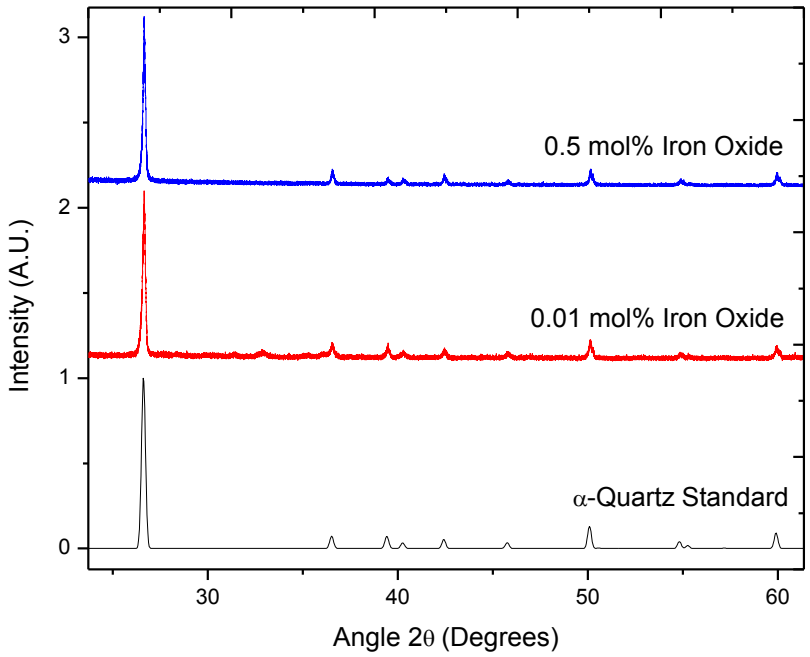

Figure 4.3.1 XRD analysis of densified core-shell powders with various iron oxide concentrations with arbitrary normalized intensity units, and a scan range from 25° to 60°

Rough density calculations were performed with known geometries and masses of samples, with sample diameter and thicknesses averaged from multiple measurements on each sample. It was found that pure silica reached higher density at lower temperatures than iron oxide-imbedded powders, with an increasing densification temperature proportional to increasing iron oxide concentrations. Relative density calculations were performed on all samples, with a focus on pure silica, 0.5 mol% samples, and 2.5 mol% samples.

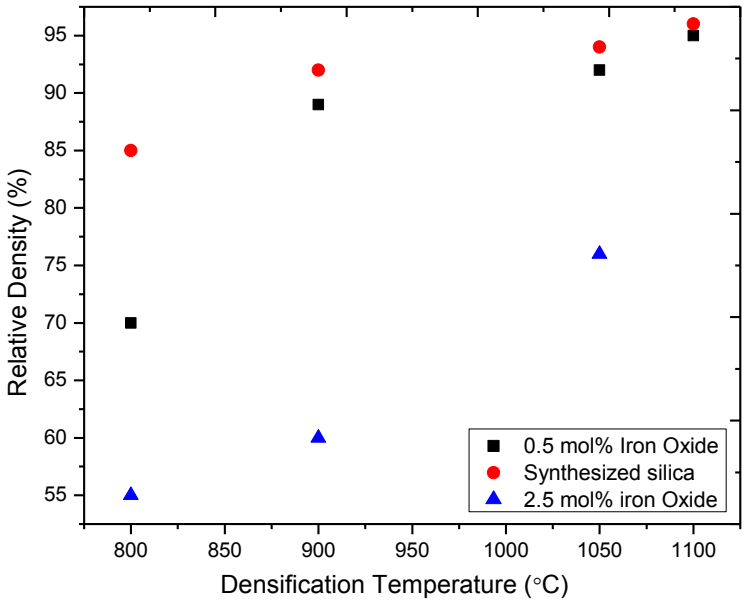

Figure 4.3.2 Relative density of 0.0 mol%, 0.5 mol%, and 2.5 mol% densified samples as a function of processing temperature

It was observed that with the same load rate, maximum load, and hold time, sample density increased as a function of temperature, with iron oxide-containing samples reaching full density at higher temperatures. While all transparent samples densified with similar trends at and above 900ºC, non-transparent samples with higher iron oxide concentration were shown to reach lower densities under similar conditions.

4.4 Transmission Measurements of Densified Samples

Transmission measurements were performed on 0.0, 0.01, 0.5, 1.0, 2.5, and 5.0 mol% iron oxide densified samples, ranging from 250nm to 900nm wavelengths, with the

primary scan range focused on the visible spectrum. Visible light transmission measurements were performed on both unpolished and polished samples. Pure silica (0.0 mol% iron oxide) exhibited the highest transmission in both unpolished and polished samples, at between 60-70% transmission of the primary visible wavelengths. At 0.5 mol% iron oxide, transmission through visible wavelengths followed a similar trend, although maximum transmission was approximately 10% lower than iron oxide-free samples. However, below the visible spectrum and entering the near-ultraviolet and ultraviolet regime, samples exhibited a rapid decline in transmission, with near-zero transmission at wavelengths below 300nm. It is believed that the loss of transmission at lower wavelengths is due to scattering effects caused by the presence of the iron oxide nanoparticles, which have a vastly different index of refraction from that of quartz.

Transmission measurements performed on the unpolished samples showed somewhat skewed transmission percentages due to the presence of unremoved graphite foil (remnants of the densification process). Polishing of the transparent samples not only removed the graphite foil on the surface of the samples, but also allowed for transmission measurements affected only by the internal structures. A drastic change was seen in measurements between unpolished and polished samples, with the highest transmission in 0.0 mol% samples, decreasing with 0.01 mol%, and the lowest transmission in 0.5 mol% samples.

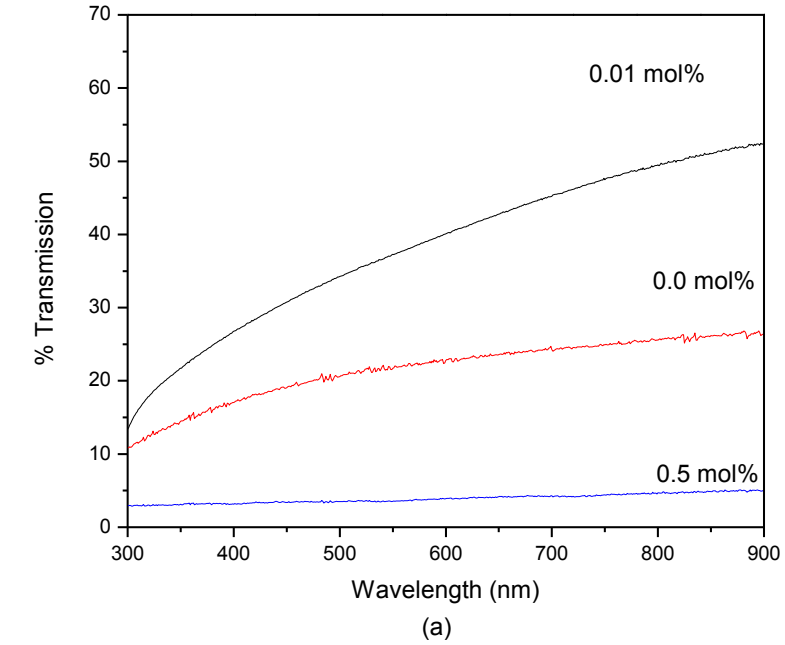

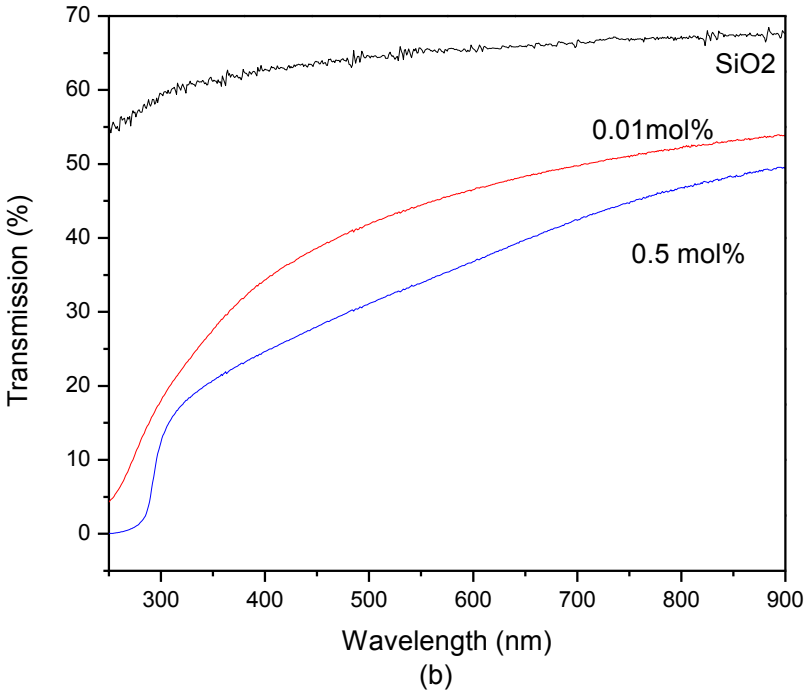

Figure 4.4.1 Transmission measurements for 0.00, 0.01, and 0.5 mol% Iron Oxide encased within silica samples in (a) unpolished and (b) polished samples, with percent transmission (y-axis) versus wavelength of light (x-axis)

Higher iron-oxide concentrations in densified samples greatly diminished visible-light transmission, with concentrations at or greater than 1.0 mol% reducing transmission to near zero. Transmission behavior between 1.0, 2.5, and 5.0 mol% samples exhibit similar trends, with a maximum of 5-6% transmission at near-infrared wavelengths, and a rapid decline to almost 0% transmission within the visible spectrum.

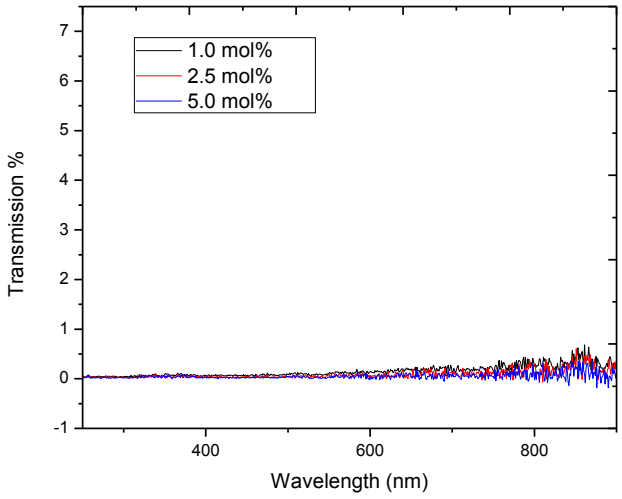

Figure 4.4.2 Transmission for 1.0, 2.5, and 5.0 mol% iron oxide ranging incased in silica from near-UV to near-Infrared

Due to the powder processing conditions, it can be assumed that carbon contamination is a contributing factor to the rapid decline in transmission with increased iron oxide concentrations. The relation between iron oxide concentration and potential carbon contamination encased within the silica matrix is nearly linear, in effect double photon scattering sites with successive increase in iron oxide within the core-shell structures.

Nonetheless, due to the reverse-micelle/core-shell powder synthesis method, it is possible to attain high transparency in visible wavelengths with iron oxide concentrations one order of magnitude higher than previously reported works[36].

4.5 Magnetic Characterization of Densified Samples

Using Vibrating Sample Magnetometry (VSM), it is possible to characterize the magnetic properties of the densified core-shell structures to determine the presence of iron oxide and a relative ratio of iron oxide to silica. Silica (SiO_2) is a diamagnetic material, due to the complete pairing of electrons within the crystal lattice, and will react to an applied magnetic field with a linearly increasing magnetic moment in opposition to the applied field direction. The presence of ferromagnetic or paramagnetic materials will therefore offset the negative-response diamagnetic moment proportionally with increasing ferromagnetic or paramagnetic concentration. With sufficiently high concentrations of iron oxide (either as γ-Fe_2O_3, Fe_3O_4 or similarly magnetic phases) it can be expected that the response of the magnetic moments to increasing field will begin to increase positively with increasing applied field.

VSM analysis was performed on three concentrations of iron oxide within silica coreshell structures – 0.0mol%, 0.01mol%, and 0.5mol% - to demonstrate the shift from diamagnetic hysteresis to a paramagnetic hysteresis. It can be seen (figure 4.5.1a) that the effect of even small concentrations (0.01 mol%) iron oxide can noticeably change the magnetic properties of a material system.

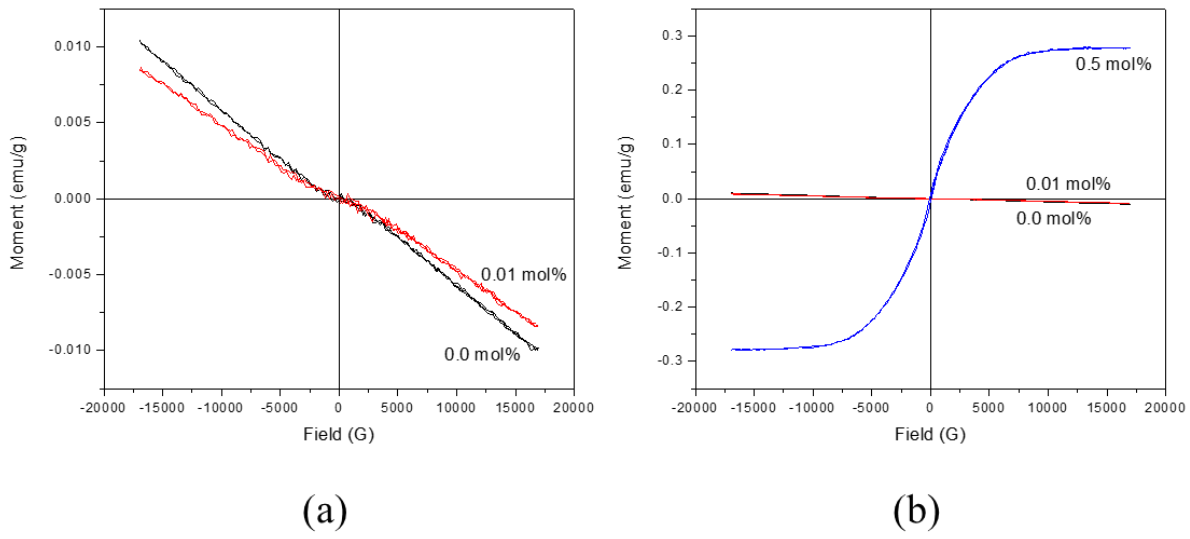

Figure 4.5.1 (a) VSM Hysteresis of pure silica (0.0mol%) and 0.01mol% Iron Oxide sample. (b) Increasing iron oxide concentration to 0.5 mol% Iron Oxide showed a drastic shift to a paramagnetic behavior

It can also be seen that the increase of iron oxide concentrations up to 0.5 mol% drastically affects the magnetic behavior of the densified samples, shifting completely from diamagnetic to a highly paramagnetic material system (figure 4.5.1b). A further consequence of the drastic effect that the presence of even low concentrations of magnetic materials can have on a composite system is that the shift in magnetic moment response can be used to roughly calculate the percentage of magnetic material. The shape of the hysteresis can also be used to estimate the phase and/or the particle size of the iron oxide. The paramagnetic hysteresis indicates either the presence of reduced iron oxide (Fe_3O_4 or magnetite) or γ-Fe_2O_3 in particle sizes below that of the critical, or single domain size, thus displaying a superparamagnetic system[37], [38]. The ability to

constrain particle size and limit grain growth are the primary reasons for choosing a core-shell synthesis process, and may contribute to the presence of superparamagnetic γ-Fe_2O_3 in the final densified system.

Chapter 5 – Summary and Conclusion

Iron oxide, exists in a variety of crystallographic polymorphs which exhibit magnetic behaviors unique from each other and is therefore a desirable material system for a variety of applications. A reverse-micelle/sol-gel process was used to synthesize iron oxide precursors with alkali ion adsorbed on the surface then further encased in a silica matrix to prevent particle aggregation and force preferential growth in the desired direction. Heat treatment was then applied to form γ-, β-, ε-, and α-Fe_2O_3 at various temperatures. Through a combination of XRD, TGA, and VSM analysis, all four polymorphs of iron oxide were characterized, with observed phase transitions occurring at approximately 780º, 940º, 1050º, and 1230ºC.

To form transparent composites with high iron oxide concentrations, a silica precursor solution was prepared, forming the external shell structure. The iron oxide precursor solution, taking the role of the core structure, was dispersed into the silica solutions, effectively forming well-dispersed, iron oxide/silica core-shell structures. Varying amounts of iron oxide precursor solution was added to obtain the desired ending concentration of iron oxide within the silica matrices. The solutions were then dried in vacuum to remove excess byproduct, then heat-treated for several hours to remove organic contamination.

The synthesized core-shell powders, with iron oxide concentrations of 0.0, 0.01, 0.5, 1.0, 2.5, and 5.0 mol% were then densified via CAPAD processing into bulk samples. CAPAD processing relies on a combination of rapid joule heating in

conjunction with a simultaneous high-pressure load to facilitate rapid densification of materials, effectively creating highly dense structures with minimal grain growth and retaining metastable phases that may otherwise be unable to exist in bulk form under conventional sintering processes. Samples with iron oxide concentrations as high as 0.5 mol% retained a high level of transparency of up to 60% transmission in visible wavelengths, which can be attributed to the combination of high dispersion and small particle size due to the core-shell synthesis method as well as the capability of retaining small grain size while simultaneously removing porosity through CAPAD processing.

Through a highly controllable and tunable chemical synthesis and processing method, it was possible to create iron oxide nanoparticles with desired phase and morphological composition. These iron oxide nanoparticles were then used to form core-shell structures by dispersing the iron oxide precursor solution into silica precursors. The iron oxide structures were dispersed during the formation of the silica shell, effectively forming well-dispersed iron oxide/silica core-shell structures. These core-shell powders were then densified via CAPAD processing, in which it was observed that samples with high iron oxide concentrations retained transparency, demonstrating the potential for such a bottom-up synthesis and processing technique in producing unique material systems for a variety of applications. Such a synthesis and processing method can be applied to multiple material systems in order to produce magnetic composites or magneto-optical materials.

References

[1] P. N. Schatz and A. J. McCaffery, “The Faraday effect,” *Q. Rev. Chem. Soc.*, vol. 23, no. 4, p. 552, 1969.

[2] H. W. Meyer, *A History of Electricity and Magnetism*. Norwalk, Connecticut: Burndy Library, 1972.

[3] D. J. Griffiths, *Introduction to Quantum Mechanics*, 2nd ed. Upper Saddle River, NJ, 2005, p. 480.

[4] C.-G. Stefanita, *Magnetism Basics and Applications*. New York: Springer-Verlag Berlin Heidelberg, 2012.

[5] S. Sakurai, A. Namai, K. Hashimoto, and S. Ohkoshi, “First Observation of Phase Transformation of All Four Fe 2 O 3 Phases,” no. 29, pp. 18299–18303, 2009.

[6] J. R. Morales, “Tailoring Magnetic Properties in Bulk Nanostructured Solids,” 2011.

[7] R. A. Swalin, *Thermodynamics of Solids*, 2nd ed. Wiley-VCH; 2 edition (December 15, 1972), 1972, p. 400.

[8] J. Tuček, R. Zbořil, A. Namai, and S. Ohkoshi, “ε-Fe 2 O 3 : An Advanced Nanomaterial Exhibiting Giant Coercive Field, Millimeter-Wave Ferromagnetic Resonance, and Magnetoelectric Coupling,” *Chem. Mater.*, vol. 22, no. 24, pp. 6483–6505, Dec. 2010.

[9] M. De Graef and M. E. McHenry, *Structure of Materials: An Introduction to Crystallography, Diffraction, and Symmetry*, 2nd ed. Cambridge University Press, 2012, p. 767.

[10] R. Gillespie and P. Popelier, *Chemical Bonding and Molecular Gemoetry - From Lewis to Electron Densities*. 2001, p. 307.

[11] J. E. Garay, “Current-Activated, Pressure-Assisted Densification of Materials,” *Annu. Rev. Mater. Res.*, vol. 40, no. 1, pp. 445–468, Jun. 2010.

[12] J. Herbst, J. Croat, F. Pinkerton, and W. Yelon, “Relationships between crystal structure and magnetic properties in Nd_{2}Fe_{14}B,” *Phys. Rev. B*, vol. 29, no. 7, pp. 4176–4178, Apr. 1984.

[13] R. Zboril, M. Mashlan, and D. Petridis, “Iron(III) Oxides from Thermal ProcessesSynthesis, Structural and Magnetic Properties, Mössbauer Spectroscopy Characterization, and Applications †,” *Chem. Mater.*, vol. 14, no. 3, pp. 969–982, Mar. 2002.

[14] J. R. Morales, “Novel Magnetic Behavior in Bulk Nanostructured Iron Oxides,” no. August, 2008.

[15] G. C. Hadjipanayis, “Nanophase hard magnets,” *J. Magn. Magn. Mater.*, vol. 200, no. 1–3, pp. 373–391, Oct. 1999.

[16] Ö. Helgason and T. I. Sigfússon, “Mössbauer spectroscopy for determining phase stability in the ferrosilicon system,” *Hyperfine Interact.*, vol. 45, no. 1–4, pp. 415–418, Mar. 1989.

[17] T. I. Sigfússon and Ö. Helgason, “Rates of transformations in the ferrosilicon system,” *Hyperfine Interact.*, vol. 54, no. 1–4, pp. 861–867, Jul. 1990.

[18] R. D. Shannon, “Refractive Index and Dispersion of Fluorides and Oxides,” *J. Phys. Chem. Ref. Data*, vol. 31, no. 4, p. 931, Dec. 2002.

[19] E. Hecht, *Optics*, 4th ed. Addison-Wesley Longman, Incorporated, 2002, 2002, p. 698.

[20] N. Mahmed, O. Heczko, R. Maki, O. Söderberg, E. Haimi, and S.-P. Hannula, “Novel iron oxide–silica coreshell powders compacted by using pulsed electric current sintering: Optical and magnetic properties,” *J. Eur. Ceram. Soc.*, vol. 32, no. 11, pp. 2981–2988, Aug. 2012.

[21] K. K. Lee, D. R. Lim, H.-C. Luan, A. Agarwal, J. Foresi, and L. C. Kimerling, “Effect of size and roughness on light transmission in a Si/SiO[sub 2] waveguide: Experiments and model,” *Appl. Phys. Lett.*, vol. 77, no. 11, p. 1617, 2000.

[22] S. Sakurai, K. Tomita, K. Hashimoto, H. Yashiro, and S. Ohkoshi, “Preparation of the Nanowire Form of ε -Fe 2 O 3 Single Crystal and a Study of the Formation Process,” pp. 20212–20216, 2008.

[23] S. Laurent, D. Forge, M. Port, A. Roch, C. Robic, L. Vander Elst, and R. N. Muller, “Magnetic iron oxide nanoparticles: synthesis, stabilization, vectorization, physicochemical characterizations, and biological applications.,” *Chem. Rev.*, vol. 108, no. 6, pp. 2064–110, Jun. 2008.

[24] A. Solids, “SOL-GEL PROCESSING II. The role of the catalyst OF SILICA,” vol. 7, 1986.

[25] S. Ohkoshi, S. Sakurai, J. Jin, and K. Hashimoto, “The addition effects of alkaline earth ions in the chemical synthesis of ε-Fe[sub 2]O[sub 3] nanocrystals that exhibit a huge coercive field,” *J. Appl. Phys.*, vol. 97, no. 10, p. 10K312, 2005.

[26] J. Wiley, *Fundamentals of Materials Science and Engineering An Interactive*. .

[27] A. Patterson, “The Scherrer Formula for X-Ray Particle Size Determination,” *Phys. Rev.*, vol. 56, no. 10, pp. 978–982, Nov. 1939.

[28] V. Kazmiruk, *Scanning Electron Microscopy*. Croatia, 2012, p. 830.

[29] R. A. Llewellyn and P. A. Tipler, *Modern Physics*, 5th ed. New York, 2008, p. 673.

[30] S. Foner, “Versatile and Sensitive Vibrating-Sample Magnetometer,” *Rev. Sci. Instrum.*, vol. 30, no. 7, pp. 548–557, 1959.

[31] F. Fiorillo, *Measurement and Characterization of Magnetic Materials*. San Diego: Elsevier Inc, 2004, p. 635.

[32] T. R. Society, R. Society, and P. Sciences, “Magnetic hysteresis and minor loops : models and experiments,” vol. 386, no. 1791, pp. 251–261, 2013.

[33] J. Nogués, J. Sort, V. Langlais, V. Skumryev, S. Suriñach, J. S. Muñoz, and M. D. Baró, “Exchange bias in nanostructures,” *Phys. Rep.*, vol. 422, no. 3, pp. 65–117, Dec. 2005.

[34] N. Keskar and J. Chelikowsky, “Structural properties of nine silica polymorphs.,” *Phys. Rev. B. Condens. Matter*, vol. 46, no. 1, pp. 1–13, Jul. 1992.

[35] S. Dutch, “Silica Polymorphs,” 2009. [Online]. Available: http://www.uwgb.edu/dutchs/Petrology/Silica Poly.HTM. [Accessed: 06-Jan-2014].

[36] N. Mahmed, O. Heczko, R. Maki, O. Söderberg, E. Haimi, and S.-P. Hannula, “Novel iron oxide–silica coreshell powders compacted by using pulsed electric current sintering: Optical and magnetic properties,” *J. Eur. Ceram. Soc.*, vol. 32, no. 11, pp. 2981–2988, Aug. 2012.

[37] J. M. D. Coey and D. Khalafalla, “Superparamagnetic γ-Fe2O3,” *Phys. Status Solidi*, vol. 11, no. 1, pp. 229–241, May 1972.

[38] K. Kluchova, R. Zboril, J. Tucek, M. Pecova, L. Zajoncova, I. Safarik, M. Mashlan, I. Markova, D. Jancik, M. Sebela, H. Bartonkova, V. Bellesi, P. Novak,

and D. Petridis, “Superparamagnetic maghemite nanoparticles from solid-state synthesis - their functionalization towards peroral MRI contrast agent and magnetic carrier for trypsin immobilization.,” *Biomaterials*, vol. 30, no. 15, pp. 2855–63, May 2009.